Simulating breaking waves and estimating loads on offshore wind turbines using computational fluid dynamic models

MA Lackner, DP Schmidt, SR Arwade
University of Massachusetts Amherst

AT Myers
Northeastern University

AN Robertson
NREL

Final Report
October, 2018

Executive summary

Offshore wind energy installations located in shallow water may encounter breaking waves. The likelihood and severity of the breaking wave impact depends on local depth, sea floor slope, and wave length. Currently, several analytical criteria may be used to estimate the occurrence of breaking waves and their slam force. This article employs two-phase CFD in order to assess the applicability of breaking wave limits. Further, the CFD predictions are compared to models of the slam force imparted by the breaking wave. We find that the Goda limit is the most accurate breaking limit for low seafloor slopes (s<8%), which are common at US East Coast sites suitable for fixed-bottom offshore wind farms. Further, the CFD simulations report lower slam forces than all of the reduced-order models considered here. Considering the comparison to CFD, the Goda slam model appears to be the least conservative and the Cointe-Armand and Wienke-Oumerachi slam models are the most conservative.

Task 1: Environmental conditions for the U.S. East Coast

The objective of Task 1 is to analyze environmental conditions for three locations along the U.S. Atlantic Coast: Georgia, New Jersey (Fishermen's Energy) and Maine. For each of the sites, seastate statistical properties are calculated for the most extreme recorded seastate, as well as a range of forecasted extreme wave heights. The range of bathymetry conditions are also examined for each site. Together, these characteristics provide guidance on conditions where breaking could occur in potential wind farms located off the U.S. East Coast.

1.1 Most extreme recorded seastate

First, yearly buoy data for the Maine and Georgia locations are obtained for all historical data that included wave spectral properties from the NOAA National Data Buoy Center [1]. The data include hourly measurements of spectral wave power at various wave frequencies. To obtain statistical wave properties such as significant wave height, various moments of the wave spectrum are computed. The zeroth spectral moment, m_0 is computed using

$$m_0 = \int S(f) \, df \tag{1.1}$$

where $S(f)$ is the wave spectral density at wave frequency f. The significant wave height is calculated as

$$H_s = 4 * \sqrt{m_0} \tag{1.2}$$

The second spectral moment is directly related to the average wave period. The second spectral moment is calculated using

$$m_2 = \int S(f) f^2 df \tag{1.3}$$

and the average wave period is calculated as

$$T_{avg} = \sqrt{m_0/m_2} \tag{1.4}$$

The peak spectral period, T_p, is equal to the inverse of the frequency corresponding to the peak in the wave spectrum. The significant wave height H_s, average wave period T_{avg}, and peak spectral period T_p are calculated at every available hour in the Maine and Georgia sites.

The wave spectrum corresponding to the most extreme hourly seastate for both sites are given in Figure 1.1, including the best fit JONSWAP spectrum for each seastate. The JONSWAP spectrum is defined as

$$S(f) = \frac{1}{2\pi} \frac{5}{16} H_s^2 T_p \left(f T_p\right)^{-5} \exp\left[-\frac{5}{4}\left(f T_p\right)^{-4}\right] [1 - 0.287 \ln(\gamma)] \gamma^{\exp\left[-0.5\left(\frac{f T_p - 1}{\sigma}\right)^2\right]} \tag{1.5}$$

where γ is the peak shape parameter, and σ is the scaling factor. As shown in Figure 1.1, the JONSWAP spectrum is a relatively good approximation of the spectra describing the most extreme recorded seastate for the Georgia and Maine sites.
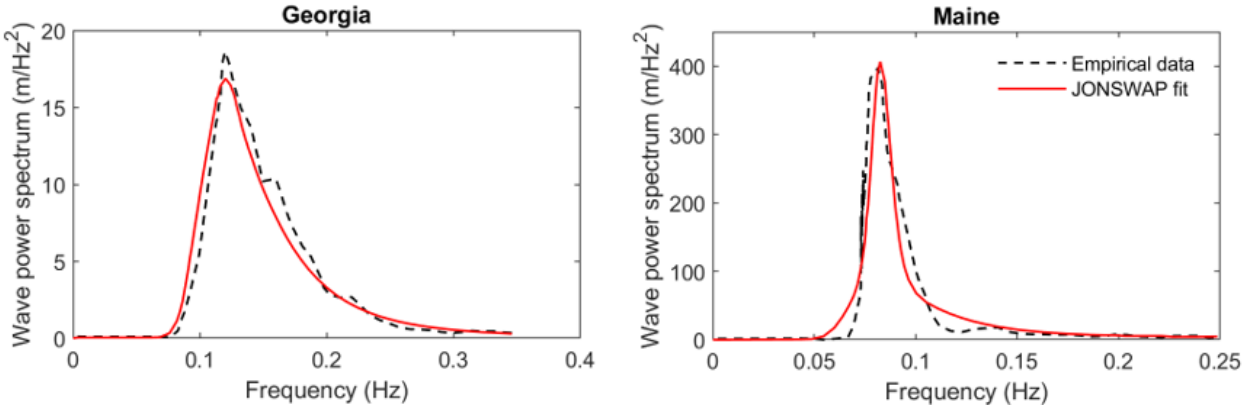
Figure 1.1: Measured (dashed black) and JONSWAP fit (solid red) for wave spectra at the Georgia and Maine sites for the highest hourly H_s in the buoy database.

For the New Jersey site, measured hourly data for the significant wave height H_s, average wave period T_{avg}, and peak spectral period T_p is obtained directly from Fishermen's Energy for a 1.5 year span in 2011 to 2012. Table 1.1 compares the hourly wave statistics recorded during the hour corresponding to the highest hourly significant wave height recorded at each site during the span of the available data for each site.

Table 1.1: Wave statistical properties for the hour corresponding to the highest recorded significant wave height H_s at each site.

Site	Buoy depth d (m)	Max. H_s (m)	T_{avg} (s) at max. H_s	T_p (s) at max. H_s
Georgia	19	4.5	6.3	8.3
New Jersey	12	6.0	6.3	13.17
Maine	23	11.8	10.9	11.8

1.2 Forecast of extreme seastates

A range of forecasted extreme seastates is derived from a combination of buoy measurements and hindcasts for each site. The buoy measurements are again obtained from the NOAA National Data Buoy Center [1], while the hindcast measurements are obtained from the U.S. Army Corps Wave Information Systems (WIS) reanalysis [2].

Wave heights are extrapolated to 50-year extreme wave height values using the Inverse First Order Reliability Method, as recommended by IEC-61400-3 guidelines for design load case 6.1 [3]. The lower bound on each wave height range is determined from the maximum wave recorded in the 30-year hindcast point closest to each site. The upper bound is determined by fitting a generalized extreme value distribution to the buoy data and extrapolating to the 50-year value. The wave periods associated with the wave height ranges are estimated using the following relationship, adapted from the IEC-61400-3 guidelines [3]:

$$11.1\sqrt{\frac{H}{g}} < T < 14.3\sqrt{\frac{H}{g}} \tag{1.6}$$

1.3 Bathymetry characterization

Water depths for the three locations are then derived from the Northeast Atlantic and Southeast Atlantic Relief Model datasets from NOAA's U.S. Coastal Relief Model [4, 5]. The bathymetric datasets are converted to raster Digital Elevation Models (DEMs) in QGIS, an open source geographic information systems software suite [6]. The raster DEMs are converted to Slope DEMs using a scale ratio of 1.00. A 10 km buffer is applied to the coordinates of interest for every location. The water depth ranges and seafloor slope ranges are then extracted from the 10 km zones surrounding the sites.

1.4 Summary of East Coast conditions

Table 1.2 summarizes the estimated ranges for 50-year extreme ocean conditions for each site off the U.S. East Coast, including water depth d, seafloor slope s, extreme wave height H, and associated period T. These ranges are used to approximate extreme ocean conditions in potential U.S. Atlantic Coast wind energy development sites.

Table 1.2: Ranges for water depth, seafloor slope, extreme wave height, and associated period for potential U.S. East Coast wind energy development sites.

Site	Depth (m)	Slope (%)	Wave height (m)	Wave period (s)
Georgia	$12 \leq d \leq 25$	$0 \leq s \leq 1$	$6 \leq H \leq 12$	$10 \leq T \leq 14$
New Jersey	$2 \leq d \leq 20$	$0 \leq s \leq 2$	$7 \leq H \leq 22$	$11 \leq T \leq 19$
Maine	$2 \leq d \leq 50$	$0 \leq s \leq 12$	$7 \leq H \leq 21$	$11 \leq T \leq 19$

Task 2: Verify and validate CFD model

The objective of Task 2 is to validate and verify the CFD model against experimental data and accepted analytical models for cases relevant to breaking wave forces on offshore wind turbine support structures. This section summarizes the four main cases used to validate and verify the Converge CFD model, with each case providing confirmation for a different aspect of modeling breaking wave forces on offshore wind support structures. These four cases are:

1. Dam break: capturing structure of a breaking water front
2. Nonlinear waves: generation, propagation, and absorption of nonlinear waves
3. Shoaling waves: ability to produce breaking waves; capture shoaling behavior
4. Force from regular waves: force on cylinder due to regular nonlinear waves

The process of validating and verifying these four cases also develops a set of "best practice" guidelines for setting parameters in the Converge CFD model for wave applications (like solver parameters, interface reconstruction models, mesh resolution, turbulence models, etc.). Additional details on each case can be found in the progress reports for quarters 1-4.

2.1 Dam break verification

The first case is the single-sided 2D dam break described by Whitman [7], where the flow is assumed to be incompressible, inviscid, and without surface tension. A column of water with height $d_0 = 50$ cm and width $w = 3$ m is initially confined on the left side of a 10 m by 60 cm domain. The column is released at the beginning of the simulation ($t = 0$ s) and allowed to collapse towards the right under the influence of gravity g.

The CFD domain is bounded by slip walls on the left and right sides as well as the bottom, with the top open to atmospheric pressure. The CFD mesh has a base cell size of $w/150$ by $d_0/100$ and adaptive mesh refinement at the interface down to a cell size of $w/300$ by $d_0/200$. The timestep size is adjusted throughout the simulation to maintain a Courant number of 0.4. The advection scheme is 1st order upwinding, with a SOR solver for momentum and a BiCGstab solver for pressure. The air-water interface is tracked using the Volume of Fluid (VOF) method with Piecewise-Linear Interface Calculation (PLIC) interface reconstruction [8].

The water depth d, as a function of distance x from the left edge of the domain and time t, is compared to the analytical solution based on potential flow theory, as discussed in Whitman [7]:

$$\sqrt{gd} = \frac{1}{3}\left(2\sqrt{gd_0} - \frac{x-w}{t}\right) \quad for \quad -\sqrt{gd_0} \le \frac{x-w}{t} \le 2\sqrt{gd_0}. \tag{2.1}$$

Figure 2.1 shows the depth d across the domain at two different times, comparing the CFD results to the analytical solution. As Figure 2.1 shows, the CFD interface shape is in excellent agreement with the analytical solution, particularly at later times when the potential flow solution is more accurate [7]. The verification of this dam break case against analytical results indicates

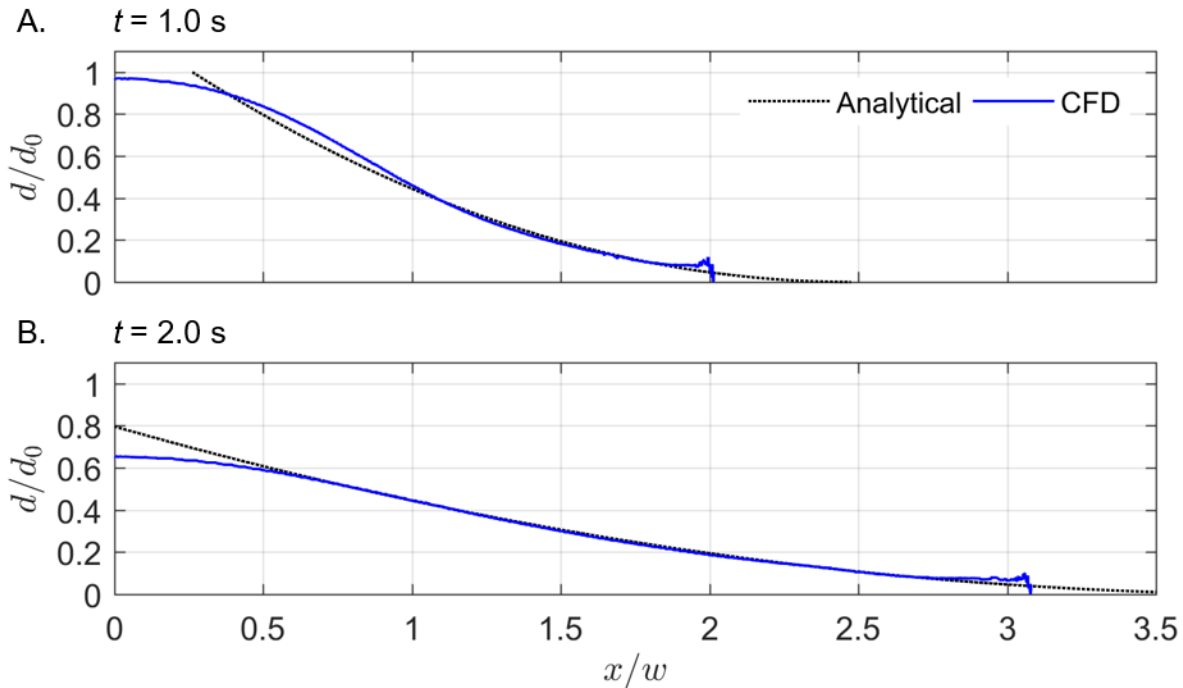that the CFD model can accurately simulate a collapsing water front, like those found in breaking waves.

A. $t = 1.0$ s

B. $t = 2.0$ s

Figure 2.1: CFD results (solid blue) and analytical results based on potential flow (dotted black) for a collapsing water column, initially w=3 m wide and d_0=50 cm tall. Water depth is plotted versus distance from the left tank wall at times of 1 s (A) and 2 s (B).

2.2 Nonlinear wave kinematics verification

The second case is the generation and propagation of 2D nonlinear regular waves. Nonlinear waves of height $H = 10$ cm, period $T = 1.0$ s, and wavelength $L = 1.62$ m are generated in a water depth of $d =1.0$ m. These waves are assumed to obey 5th order Stokes wave theory, described by Fenton [9, 10]. Figure 2.2 illustrates the case setup.

The CFD domain is 5 m long and 1.5 m tall, with slip walls on the top and bottom. The waves are generated by prescribing the velocity and surface elevation at the left "inlet" boundary (calculated according to 5th order Stokes wave theory), with a Neumann condition on pressure. The domain is also initialized with pressure, velocity, and surface elevation distributions calculated according to 5th order Stokes wave theory.

At the right "outlet" boundary, a hydrostatic pressure distribution is prescribed, with a Neumann condition on velocity. To prevent unphysical reflections off the outlet boundary, a momentum damping region is introduced to for the rightmost 1 m of the domain (see Figure 2.2) by adding a sink term -$S\rho u$ to the Navier-Stokes equation. The positive sink coefficient S increases quadratically from the beginning of the damping region to create a smooth transition between the damped and non-damped regions.
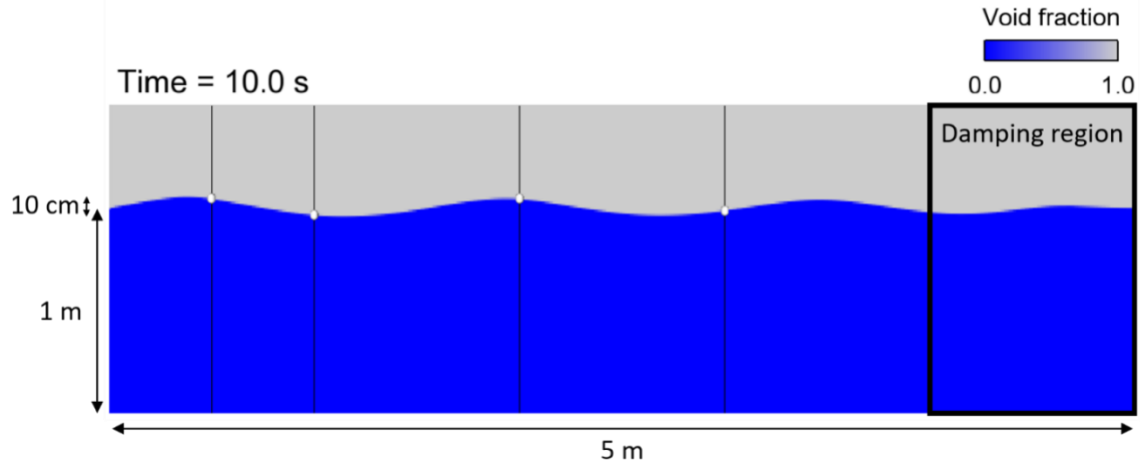
Figure 2.2: CFD simulation of 5th order Stokes waves (H=10 cm, d=1 m, T=1 s) shown at time 10 s. The 2D domain is 5 m long, with a 1 m momentum damping region at the outlet on the right. The surface elevation is measured at 0.5, 1, 2, and 3 m from the inlet on the left, indicated by white dots.

The CFD mesh has a base cell size of $L/20$ by $d/12.5$, with adaptive mesh refinement at the interface down to a cell size of $L/160$ by $H/10$. The timestep was adjusted to maintain a Courant number of 0.75. As with the dam break case, 1st order upwinding is used with SOR for momentum and BiCGstab for pressure. The VOF method with PLIC interface reconstruction is again used to track the air-water interface [8].

Figure 2.3 shows the surface elevation η as a function of time t at 1 m = 0.62L from the left "inlet" boundary (Figure 2.3A) and at 3 m = 1.85L from the left "inlet" boundary (Figure 2.3B). As shown in Figure 2.3, the CFD surface elevations match the analytical 5th order Stokes solution within the size of one cell (*0.1H*), though the agreement deteriorates farther from the left "inlet" boundary, likely due to the numerical viscosity introduced by the 1st-order advection scheme. Similar trends are observed in the surface elevations for locations 0.5 m and 2 m from the inlet.

Figure 2.4 shows the satisfactory agreement between analytical (Figure 2.4A) and CFD (Figure 2.4B) results for horizontal particle velocity at $t = 10$ s. As with the surface elevation, the CFD velocity profile becomes less accurate farther from the left "inlet" boundary. The vertical particle velocity and pressure distribution also show reasonable agreement between the CFD and analytical results, again with poorer agreement far from the inlet.

Overall, the CFD results agree reasonably well with the analytical solution derived from 5th order Stokes wave theory. This case confirms the CFD model's ability to generate and propagate nonlinear waves accurately, including the absorbtion of nonphysical waves by a momentum damping region. However, the case's decreasing accuracy far from the inlet could likely be improved by using a higher-order advection scheme.

A similar wave generarion and propagation case was also performed using 25th order stream function theory as described by Fenton [11] to generate highly nonlinear waves. This case verified the approach of prescribing wave kinematics from stream function theory.
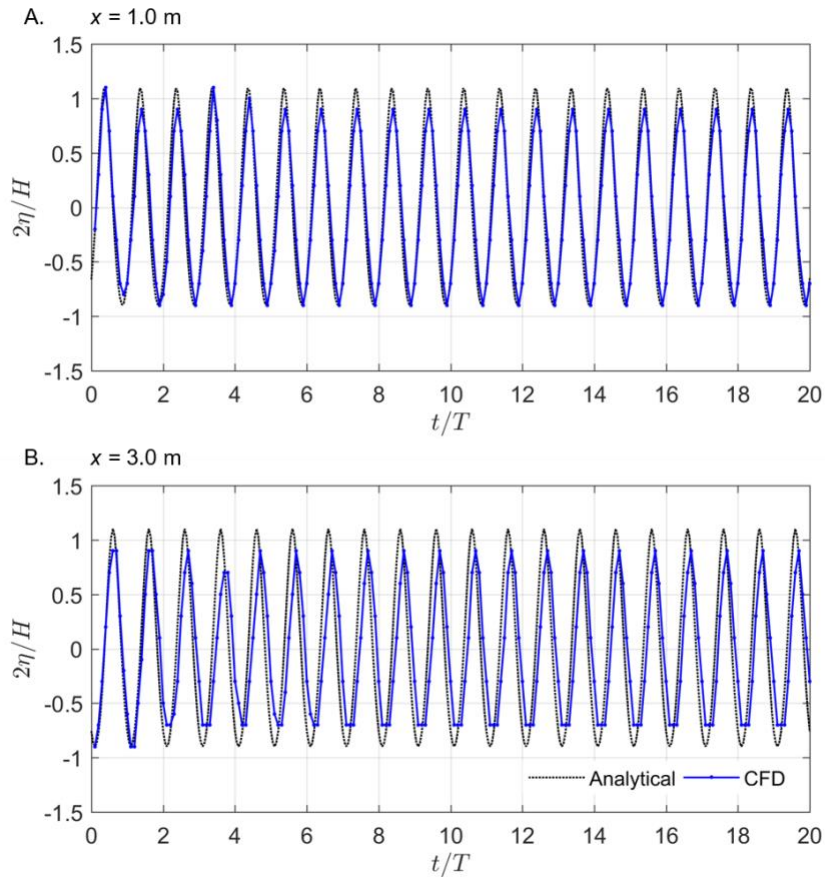
Figure 2.3: Time history of the surface elevation for 5th order Stokes waves, at locations of 1 m (A) and 3 m from the "inlet" boundary (B). CFD results are plotted in solid blue while analytical results are in dotted black.
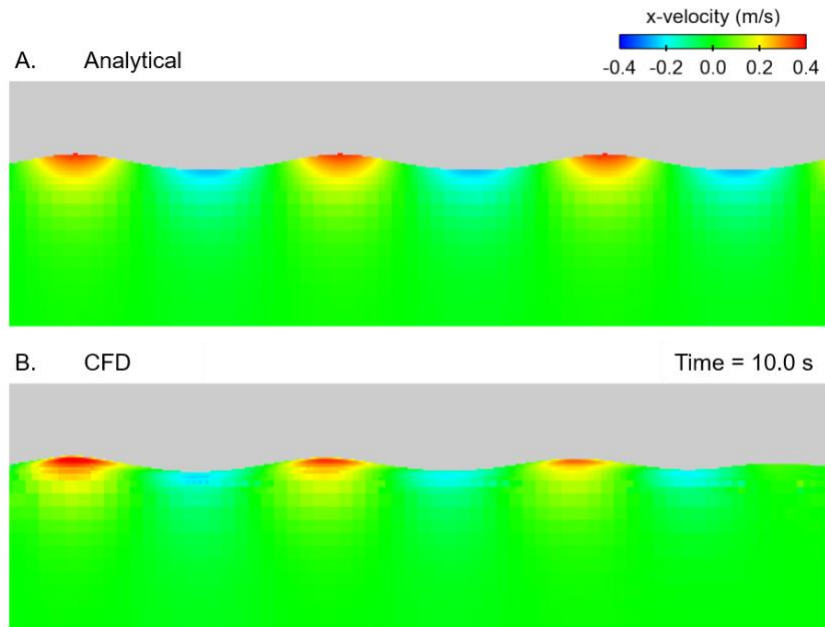

Figure 2.4: Horizontal fluid velocity at time t=10 s according to the analytical 5th order Stokes solution (A) and the CFD results (B).

2.3 Shoaling waves validation

The third case considers regular waves and a solitary wave shoaling over a sloped floor. CFD surface elevations for both regular and solitary waves are validated against experimental data from calibration tests run in the Large Wave Flume at the O.H. Hinsdale Wave Research Facility at Oregon State University.

For the regular waves case, regular nonlinear waves of height $H = 16$ cm, period $T = 2.5$ s, and wavelength $L = 8.8$ m are generated in a water depth $d = 2.15$ m. For the solitary wave case, an error function solitary wave of height $H = 51$ cm, time width $T = 10$ s, and nominal wavelength $L = 48$ m (twice the horizontal width of the wave) is generated in a water depth of $d = 2.00$ m.

The experimental flume is 87 m long, 3.7 m wide, and 4.6 m tall, with a piston wavemaker capable of generating unidirectional waves at one end and an artificial beach at the other end. Figure 2.5 shows a side view of the flume during the solitary wave case, where the wavemaker is on the left. The flume floor includes a slope starting 14.1 m from the wavemaker and ending 43.4 m from the wavemaker, so that the deep end of the flume near the wavemaker is 1.75 m deeper than the shallow end near the artificial beach.

The CFD wavemaker generates waves by moving horizontally according to the experimental displacement time history. However, the CFD domain is shortened to 87 m long, 0.5 m wide, and 3 m high, with slip walls on the front and back boundaries to create a 2D domain in keeping with the unidirectional nature of the waves. The entire length of the flume is simulated to replicate wave reflections off the beach and seiche behavior in the flume. The CFD wavemaker, floor, and right boundary are no-slip walls, while the top of the domain is open to the atmosphere.
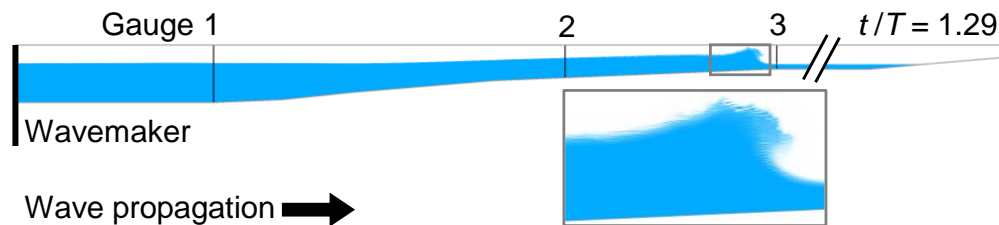

Figure 5: Partial side view of a CFD simulation of a solitary wave in the OSU Large Wave Flume at the time of breaking. The wavemaker is on the left edge and the artificial beach is on the right. 3 wave gauges are located at the start of the slope (gauge 1), on the slope (gauge 2), and at the end of the slope (gauge 3).

For the regular waves case, the CFD mesh consists of cells $L/110$ by $d/215$, with adaptive mesh refinement at the interface to a cell size of $L/440$ by $H/64$. The same mesh settings are used for the solitary wave case, so that the solitary wave interface is refined to $H/204$. For both cases the timestep is adjusted to maintain a Courant number of 0.2.

The CFD model again uses used with SOR for momentum and BiCGstab for pressure. Improving upon the previous verification cases, the momentum interpolation uses a blended Monotonic Upstream-Centered Scheme for Conservation Laws (MUSCL) interpolation scheme,

with a van Leer flux limiter [8]. The VOF method with High Resolution Interface Capturing (HRIC) interface reconstruction is used to track the air-water interface; unlike PLIC, HRIC conserves mass in cases with moving boundaries, like the wavemaker [8].

To validate the regular waves and solitary wave cases, the CFD and experimental surface elevations η are compared at three wave gauges at different locations along the flume. Wave gauge 1 is 14.172 m from the wavemaker at the start of the slop, wave gauge 2 is 32.326 m from the wavemaker on the slope, and wave gauge 3 is 43.431 m from the wavemaker at the end of the slope. Figure 2.5 shows the location of each wave gauge.

Figure 2.6 shows the surface elevation η time history for the regular waves case at each wave gauge. The CFD surface elevations are inherently imprecise because the interface is diffused over several cells. The CFD "average" surface elevation is the average location of all cells with a void fraction of 0.5, halfway between the void fraction of water (0.0) and air (1.0). The reported CFD diffuse interface represents all cells that are neither fully water ($\alpha = 0.0$) nor fully air ($\alpha = 1.0$). HRIC interface reconstruction tends to create more diffuse interfaces like those seen in this validation case [8].

As shown in Figure 2.6, the CFD surface elevations agree with the experimental surface elevations within the CFD diffuse interface. The CFD period is in excellent agreement with the experimental period at all three wave gauges. However, the CFD model tends to slightly overpredict the surface elevation, although the CFD heights accurately increase with the decrease in water depth (shoaling). Note that at gauge 3 in Figure 2.6, the experimental instrumentation is unable to measure surface elevations less than zero at wave gauge 3 and therefore cannot accurately capture the wave troughs.
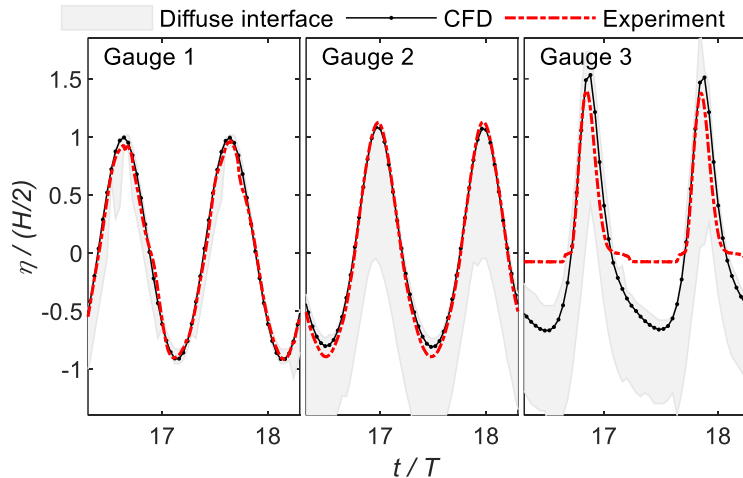

Figure 2.6: Surface elevation time histories for the regular waves case, at wave gauge 1 (left), wave gauge 2 (middle), and wave gauge 3 (right). The experimental results are in dashed red, the CFD reported interface in solid black, and the CFD diffuse interface band shaded in grey. The experimental wave gauge 3 measurements (right) are inaccurate in the wave troughs.
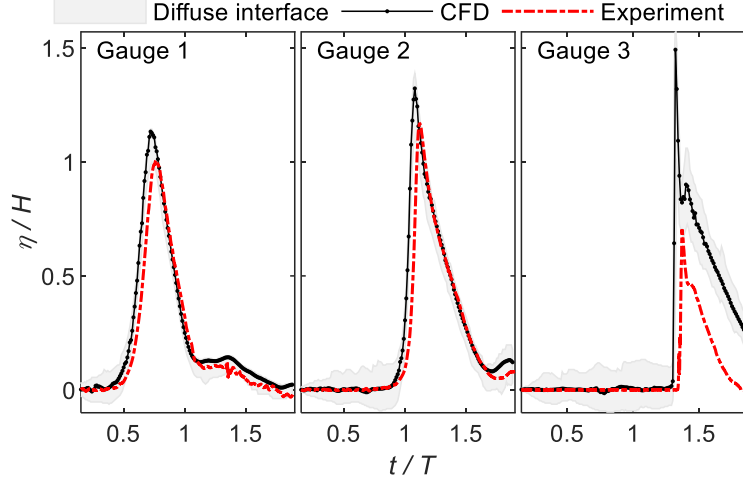
10

Figure 2.7: Surface elevation time histories for the solitary wave case, at wave gauge 1 (left), wave gauge 2 (middle), and wave gauge 3 (right). The experimental results are in dashed red, the CFD reported interface in solid black, and the CFD diffuse interface band shaded in grey. The wave is breaking at wave gauge 3 (right), making it difficult to track both CFD and experimental surface elevations.

Figure 2.7 compares the CFD and experimental surface elevations for the solitary wave case at the three wave gauges, similar to Figure 2.6 for the regular waves case. As shown in Figure 2.7, the CFD results tend to overpredict the surface elevation, though the peak height is within the CFD uncertainty at wave gauges 1 and 2. Again, the CFD wave exhibits reasonable shoaling as it moves along the slope. The CFD results also slightly overpredict the celerity and the nominal period so that the wave arrives at a given wave gauge sooner and lasts longer at a given location than in the experimental results.

In Figure 2.7, the CFD and experimental results at wave gauge 3 show poor agreement, particularly in peak surface elevation. At this location, the wave is a plunging breaker in the process of collapsing (note the lower peak height at wave gauge 3 compared to wave gauge 2). The collapsing wave produces spray, an air-water mixture that the experimental gauge struggles to capture. The CFD diffuse interface includes the modeled version of this spray. The diffuse interface band is therefore larger at gauge 3, when the wave is breaking, than at gauges 1 or 2 (see Figure 2.7). In this case, the bottom of the CFD diffuse interface band is a better approximation for the experimental gauge measurement, which largely neglects the spray. When the diffuse interface bottom is used for the CFD surface elevation, the CFD overpredicts solitary wave peak elevation by 14.2 cm (+39.4%).

Table 2.1. Difference between CFD and experiment for wave height H, *period* T *(regular waves), and peak surface elevation* η *(solitary wave) at each wave gauge.*

Gauge	Regular, H (cm)	Regular, T (ms)	Solitary, peak η (cm)
1	0.5 (+3.5%)	45.0 (+1.8%)	6.4 (+12.5%)
2	-1.1 (-6.9%)	0.2 (+0.01%)	7.8 (+13.1%)
3	1.0 (+9.5%)	0.0 (0.0%)	40.2 (+112%)

Table 2.1 further quantifies the disagreements between the CFD and experimental results shown in Figures 2.6-2.7. Overall, the CFD model satisfactorily predicts the wave height of regular nonlinear and solitary waves, including waves shoaling over a sloped bottom. In the solitary case, the model also predicts a breaking wave due to shoaling at roughly the correct location and time. The CFD model agrees well with the experimental period for regular waves, but slightly overpredicts the experimental period and celerity for the solitary wave. This validation case confirms that the CFD model can accurately shoal a nonlinear wave train and produce a breaking wave due to shoaling.

2.4 Wave force validation

The final case validates the CFD force on a cylinder due to regular waves against experimental work by Niedzwecki and Duggal [12]. Niedzwecki and Duggal measure the inline forces on a cylinder of diameter 11.4 cm subjected to regular waves with periods $T = 0.5$-1.5 s and wave heights $H = 1.04$-12.69 cm. The experiments are carried out in a wave flume 37 m long, 0.91 m wide, and 1.22 m tall, filled to a water depth $d = 0.91$ m with wave absorption provided by a 1:3.5 slope placed after the cylinder.

In the CFD simulations, the domain is reduced to 5-6 wavelengths long, 0.91 m wide, and 1.0 m tall, in order to reduce computational cost. The simulations include a dynamic Smagorinsky LES turbulence model with a Werner-Wengle wall model on the cylinder. The domain bottom and crossflow sides are no-slip walls, with the top open to atmospheric pressure. The domain sides in the direction of wave propagation are used to generate and absorb the waves.

The CFD regular waves are generated by prescribing the velocity and void fraction at a location of 1-2 wavelengths upstream of the cylinder, according to 5th order Stokes wave theory [9, 10]. The domain is also initialized with velocity, pressure, and void fraction distributions according to 5th order Stokes wave theory. Wave absorption is provided by a momentum damping region 1-2 wavelengths long, located 2-3 wavelengths downstream of the cylinder. This approach to generating and absorbing nonlinear waves is based on the approaches verified in the nonlinear waves case (case 2 of task 2).

The CFD mesh consists of base cells with an approximate size of $L/10$ by $L/10$ by $d/22$. Adaptive mesh refinement adds cells of size $L/180$ by $L/180$ by $H/20$ at the interface, and four layers of $a/45$ by $a/45$ by $H/80$ cells are also added to the cylinder surface. This mesh is selected after a brief mesh convergence study shows that halving the dimensions of the base and cylinder cells yields minimal improvements to the force results, while doubling the cell dimensions creates significant noise in the force results. Like in the previous validation and verification cases, the timestep is adjusted to maintain a Courant number of 0.4. 1st order upwinding is again used with SOR for the momentum solver and BiCGstab for the pressure solver. The VOF method with PLIC interface reconstruction is used to track the air-water interface.

The CFD simulations focus on five of the fifteen wave parameter combinations studied by Niedzwecki and Duggal. Each CFD case simulates waves of a different period, with wave heights in the range described by Niedzwecki and Duggal for that period. See Table 2.2 for a summary of the five CFD wave parameter combinations. Niedzwecki and Duggal characterize

the waves by the scatter parameter *ka*, the product of the wavenumber *k* and the cylinder radius *a* = 5.7 cm, representing a ratio of cylinder size to wavelength.

Table 2.2: Wave parameters for the CFD regular wave force cases. Wavelength and wavenumber are calculated according to 5th order Stokes wave theory [9, 10].

Scatter parameter *ka*	0.112	0.253	0.399	0.627	0.895
Wave period *T* (s)	1.47	0.947	0.749	0.595	0.498
Wave height *H* (cm)	4.93	4.65	4.43	3.29	2.25
Wavelength *L* (m)	3.12	1.41	0.897	0.571	0.400
Wavenumber *k* (m^{-1})	1.96	4.44	7.00	11.0	15.7

The force on the cylinder is characterized by the maximum inline force F_{inline} on the cylinder, averaged over several waves, in keeping with Niedzwecki and Duggal. Figure 2.8 plots the maximum inline force against the scatter parameter *ka* from the CFD simulation, Niedzwecki and Duggal's experiments, and the results of linear diffraction theory as described by Niedzwecki and Duggal [12].

As shown in Figure 2.8, the CFD force agrees very well with the experimental and theoretical values for *ka* less than about 0.7. For larger *ka,* the CFD force is significantly larger than the experimental and theoretical results. However, note that the experimental results vary considerably for a given *ka* depending on the wave height, although the CFD *ka* = 0.895 case is outside the experimental range given for nearby *ka*. Despite this, the CFD model's success at low *ka* is encouraging, since ocean waves tend to have low *ka* due to their large wavelengths compared to the scales of offshore wind support structures.

Overall, the validation of CFD regular wave forces against experimental data indicates that the CFD model accurately predicts the forces on cylindrical structures due to wave trains, especially for scales relevant for offshore wind energy.
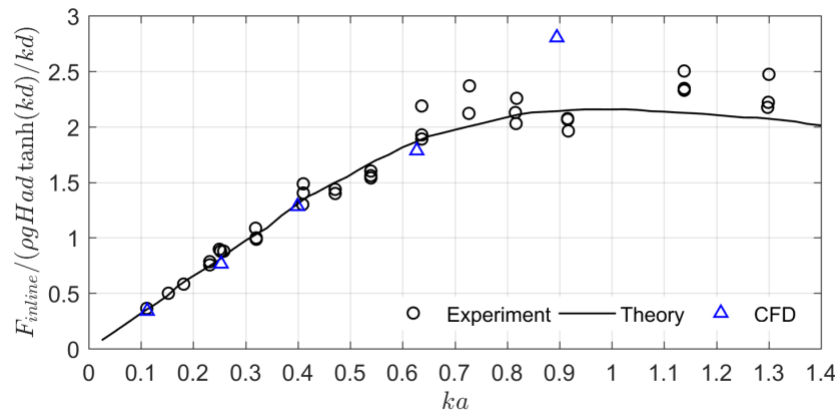

Figure 2.8: The maximum inline force on a cylinder due to regular waves, plotted versus the product of wavenumber and cylinder radius ka. *The CFD results (blue triangles) agree reasonably well with experimental values from [12] (black circles) and results from linear diffraction theory (solid black line), particularly for* ka < 0.7.

13

Task 3: CFD simulations of breaking waves

The objective of Task 3 is to examine breaking and near-breaking waves in the absence of structures, specifically for ocean conditions representative of East Coast offshore wind development sites. CFD simulations of regular wave trains shoaling and eventually breaking are performed for 39 combinations of wave height, wavelength, water depth, and seafloor slope. The results of these simulations are then compiled into a database of breaking and non-breaking waves, used to evaluate the accuracy of breaking wave limits in Task 5.

3.1 Setup of CFD simulations

Each simulated wave train is characterized by four parameters: the nominal water depth d_0, the seafloor slope s, the nondimensionalized wave height H_0/d_0, and the nondimensionalized wavelength L_0/d_0. The wave trains are simulated in a 2D computational domain with a sloping floor dictated by s. For runs with $s > 0$, the domain floor slopes upward from a depth of $1.75d_0$ at the left end of the domain to a depth of $0.25d_0$ at the right end of the domain, with the nominal depth d_0 occurring at the midpoint of the slope.

The wave trains are generated by prescribing the surface elevation and fluid velocity at the left end of a still domain. These prescribed wave kinematics are calculated using 25th order stream function theory [11] for a wave of height H_0 and wavelength L_0 in water of constant depth $1.75d_0$ (for $s > 0$) or d_0 (for $s = 0$). Although these wave kinematics are not accurate for the entire sloped-floor domain, they generate waves of initial height H_0 and initial wavelength L_0 that shoal (and sometimes break) as they move across the sloped floor.

Figure 3.1: Domain setup for a wave train with nominal depth $d_0 = 35$ m, *seafloor slope* $s = 6\%$, *nondimensionalized wave height* $H_0/d_0 = 0.50$, *and nondimensionalized wavelength* $L_0/d_0 = 9$. *Waves are generated at the left edge.*

The CFD simulations use VOF with the PLIC interface tracking scheme and a Courant number of 0.2, as recommended by the shoaling wave validation case in Task 2. Likewise, the momentum interpolation uses a blended Monotonic Upstream-Centered Scheme for Conservation Laws (MUSCL) interpolation scheme, with a van Leer flux limiter [8]. The CFD mesh resolution is based on the meshes found to give accurate results in the shoaling wave validation case in Task 2: the base cell size is approximately $L_0/100$ by $d_0/160$ or smaller, with $L_0/200$ by $H_0/110$ or smaller cells at the interface.

3.2 Selection of parameter values

Values for the nominal depth d_0 and the seafloor slope s are chosen based on representative ranges for U.S. wind energy development sites off Georgia, New Jersey, and Maine, listed in Table 1.2. The values for the nondimensionalized wave height H_0/d_0 and wavelength L_0/d_0 are chosen so that some, but not all, of the generated wave trains should break at the nominal depth d_0. The ranges chosen are therefore $0.50 \leq H_0/d_0 \leq 1.15$ and $5 \leq L_0/d_0 \leq 14$.

Note that the simulation wave heights H_0 produced by this range of H_0/d_0 often exceed the extreme wave heights for the three U.S. offshore wind energy development sites listed in Table 1.2. However, these large heights are necessary to examine breaking criteria. While the simulated water depths and slopes are based on the U.S. sites data, the simulated wave heights and wavelengths are aimed at creating breaking waves rather than matching the U.S. sites data.

Table 3.1 summarizes the wave train generation parameters d_0, s_0, H_0/d_0, and L_0/d_0 for each simulation. Some combinations of the selected parameter values could not be successfully simulated, because a consistently physical stream function solution could not be found for that combination so that a wave train could not be generated. These combinations are not included in Table 3.1.

Table 3.1: Task 3 simulated wave trains, organized by seafloor slope s, *nominal depth* d_0, *generated wave height* H_0, *and generated wavelength* L_0.

d_0 (m)	s (%)	H_0/d_0	L_0/d_0	d_0 (m)	s (%)	H_0/d_0	L_0/d_0
0	5	1.10	11	6	25	0.80	11
0	10	0.55	14	6	35	0.50	9
0	20	0.70	6	8	10	1.15	8
0	25	0.50	13	8	20	1.00	10
0	30	0.85	10	8	30	0.70	12
0	35	0.65	7	8	40	0.55	6
0	40	1.00	8	8	50	0.85	14
0	45	0.80	9	9	5	0.50	5
0	50	1.15	12	9	15	0.80	7
2	10	0.70	10	9	25	0.95	9
2	30	0.55	8	9	45	0.65	11
2	40	0.85	12	11	20	0.55	12
3	5	0.65	9	11	40	1.15	10
3	15	0.50	11	11	50	0.70	8
3	45	0.95	13	12	5	0.80	13
5	20	0.85	8	12	15	1.10	9
5	40	0.70	14	12	25	0.65	5
5	50	0.55	10	12	35	0.95	11
6	5	0.95	7	12	45	0.50	7
6	15	0.65	13				

3.3 Analysis of simulated waves

While each wave train is defined by nominal characteristics d_0, s, H_0/d_0, and L_0/d_0, individual waves within that train develop new characteristic values as they shoal and break. Therefore, breaking and non-breaking waves are characterized using local, instantaneous values d, H, and L rather than the wave train's nominal values. The seafloor slope s is consistent between the nominal wave train and each individual wave.

It is difficult to capture the exact instant of breaking in the CFD simulations, so the local instantaneous parameters d, H, and L are averaged from two times for breaking waves: immediately before the wave tongue curls over, and as the wave tongue begins to curl over. For wave trains where no waves break within the simulated time, the local instantaneous parameters are taken from the steepest non-breaking wave at the end of the simulation. The deep water wavelength L_0 is assumed to be the unshoaled wavelength prescribed at the left end of the domain.

The simulated waves are highly nonlinear and often asymmetric, as illustrated in Figure 3.2. Characterizing the local, instantaneous d, H, and L is ambiguous due to the wave's asymmetry (see Figure 3.2). In this study, the depth d is defined as the still water depth at the location of the wave's peak. The height H can be defined in three ways:
1. H_{left}, the vertical distance between the left trough and the peak of the wave,
2. H_{right}, the vertical distance between the right trough and the peak, or
3. H_{avg}, the average given by $(H_{left} + H_{right}) / 2$.

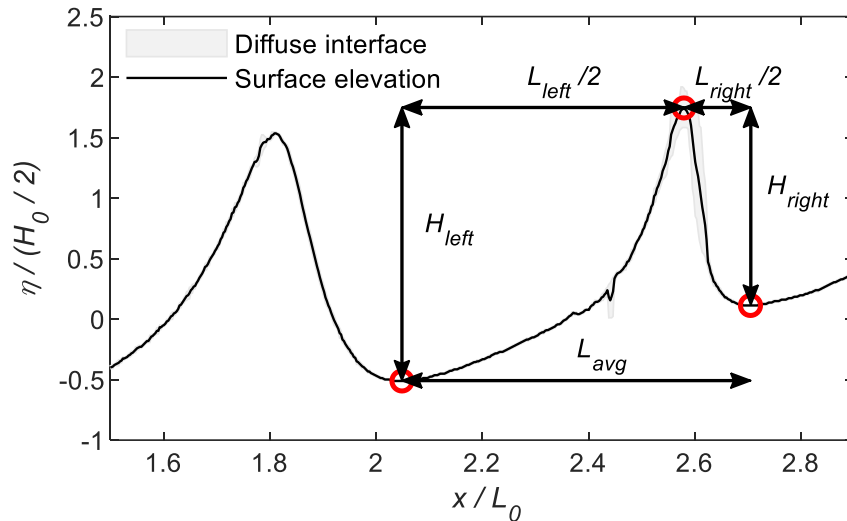The vertical arrows in Figure 3.2 illustrate H_{left} and H_{right}.

Figure 3.2: Instantaneous surface elevation of a CFD wave about to break, with its peak and troughs circled and different options for wavelength and height characterizations labeled.

Similarly, the local, instantaneous wavelength L can be defined as:
1) L_{left}, twice the horizontal distance between the left trough and the peak of the wave,
2) L_{right}, twice the horizontal distance between the right trough and the peak, or
3) L_{avg}, the horizontal distance between the left and right troughs.

The horizontal arrows in Figure 3.2 illustrate L_{left}, L_{right}, and L_{avg}. Of these three options, L_{avg} is most consistent with observations of physical asymmetric waves, since measuring trough-to-trough makes no assumptions about the symmetry of the wave.

3.5 Breaking wave database

Overall, 39 different combinations of wave height, wavelength, water depth, and seafloor slope are simulated, representing conditions similar to the U.S. East Coast sites examined in Task 1.

These simulations produced 25 breaking waves and 19 non-breaking waves, listed in Appendix A by their local instantaneous characteristics. Appendix A uses the average wave height H_{avg} and average wavelength L_{avg} unless otherwise noted.

Task 4: CFD simulations of breaking wave interactions with support structures

The objective of Task 4 is to examine the interaction of breaking waves with support structures for offshore wind turbines. CFD simulations are performed for regular wave trains shoaling over a sloped floor until the waves break on or shortly before the support structure. A total of 4 different combinations of wave height, wavelength, and support structure design are considered. The surface elevations and the forces on the support structures are then compiled into a database of breaking wave loads.

4.1 Support structures description

Two different support structures for offshore wind turbines are examined: a monopile for the DTU 10 MW reference turbine [13] and the UpWind reference monopile for the UpWind 5 MW turbine [14]. The simulated 5 MW and 10 MW untapered monopiles have diameters D of 6 m and 9 m respectively [13, 14], and are designed for 25 m of water depth.

Both structures are simulated as fixed rigid bodies, removing the need to simulate each structure's below-mudline embedded pile. The simulations also do not include any transition pieces, platform decks, or towers, in favor of isolating the breaking wave interaction with the substructure. Both monopiles are extended at a constant diameter to a length of 45 m above the sea floor, to capture impact forces from the large breaking waves. Although this extended height is larger than the height specified in the original designs [13, 14], it represents well-designed structures that avoid deck slamming during the highest wave.

4.2 CFD model parameters

As in Task 3, the two-phase CFD simulations use a Volume of Fluid (VOF) approach with the PLIC interface tracking scheme. The momentum interpolation scheme is full upwinding with a Courant number of 0.9, due to improvements to the VOF portion of the CFD code since the completion of Task 3 [8].

No turbulence model is included due to the numerical diffusion supplied by the full upwinding scheme. Slip wall boundary conditions are then applied to the domain floor and the structure, which neglects the viscous force on the structure. This is justified by Task 2 simulations of regular waves on cylinders which indicate that pressure forces are significantly larger than viscous forces, even for waves with no slamming impact force.

The CFD mesh resolution is similar to those in Tasks 2 and 3. The base cell size is approximately $L_0/120$ by $L_0/120$ by $d/150$ or smaller, with $L_0/240$ by $L_0/240$ by $H_0/170$ or smaller cells at the interface. Additional refinement is added to the structure, creating cells of width $D/120$ for the 10 MW monopile and $D/80$ for the 5 MW monopile. These cell sizes create meshes with about 14 million cells for the monopile simulations.

4.2 Setup of CFD domain

The wave trains are simulated in a 3D computational domain with a sloping floor dictated by seafloor slope s. The setup of each individual simulation is determined by the support structure type. The water depth at the structure is chosen to be 25 m ± 5 m for the monopiles to reasonably match the design depth for each structure. This monopile depth is also very reasonable for the U.S. East Coast when compared to the site ranges in Table 1.2. The depth at the left end of the domain is 40 m for the monopiles. The seafloor slopes upward to a depth of 20 m for the monopiles at the right end of the domain, as illustrated in Fig. 4.1.

As in Task 3, the wave trains are generated by prescribing the surface elevation and fluid velocity at the left end of a still domain. These prescribed wave kinematics are calculated using 25th order stream function theory [11] for a wave of height H_0 and wavelength L_0 in water of constant depth $d_0 = 40$ m for monopiles (see Fig. 4.1). The unshoaled wave height H and wavelength L_0 are selected based on Task 3 simulations to produce breaking near the structure's design depth.

Like in the Task 3 simulations, an L_0-long momentum damping zone with a horizontal floor is added to the right end of a domain, as shown in Fig. 4.1. A hydrostatic pressure gradient based on the still water depth is then applied to the right boundary.

The width of the 3D domain is based on the structure width; the domain width is five times the monopile diameter. The prescribed wave kinematics are uniform across the width of the domain, creating waves that are largely 2D until they interact with the structure. Symmetry boundary conditions are applied to the domain sides to minimize the sides' effect on the simulation.
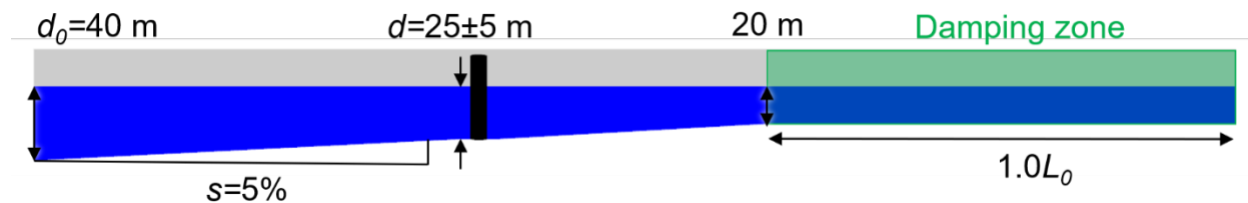

Figure 4.2: Side view of the domain setup for a simulation with a monopile. Waves are generated at the left edge, with a momentum damping zone at the right edge.

Preliminary 2D simulations without structures are conducted with different seafloor slopes s, for each unique combination of water depth, wave height H_0, and wavelength L_0. Based on these preliminary simulations, the chosen value of $s=5\%$ is found to produce breaking waves near the desired depths, with reasonable values for the wave height at breaking H and the wavelength at breaking L.

The preliminary simulations also estimate the location where waves break for a given wave height H_0, wavelength L_0, and support structure type. For the 3D simulations, the upstream edge of the structure is located at this estimated breaking location (for waves breaking on the structure), or two structure widths downstream of this estimated breaking location (for waves breaking before the structure).

19

The first portion of Table 4.1 summarizes the domain parameters for each of the four simulations. Note that the 5 MW and 10 MW monopiles are subjected to the same wave train, in order to compare the effect of structure size. Similarly, the 10 MW monopile is subjected to the same wave at different locations relative to the 2D predicted breaking location, in order to compare the effect of breaking location.

4.4 Breaking wave loads and wave characteristics

During each simulation, a time history of the force vector on the structure is recorded. Snapshots of the surface elevation around the cylinder, pressure on the cylinder, and fluid velocity within the wave are also captured throughout the simulations. Table 4.1 lists the wave characteristics derived from these surface elevation snapshots at the time just before breaking and the time of impact on the structure, using the average values for H and L (see section 3.3).

The horizontal location of the peak x_b at the moment just before it breaks (when d_b, H_b, L_b are measured) and the horizontal location of the peak x_i at the moment of impact (when d_i, H_i, L_i are measured) are also compared for the full 3D simulations. The values of $x_i - x_b$ reported in Table 4.1 therefore reflect the horizontal distance between when the wave starts to break and when the wave impacts the structure.

Figure 4.3 shows a 2D side view of each wave just before it impacts the structure. Runup on the leading edge of the cylinder is evident in all four cases. Most notably, however, simulations #2 and #3 are farther along in the breaking process than simulations #1 and #4, so that more of the crest is moving as a vertical wall of water.
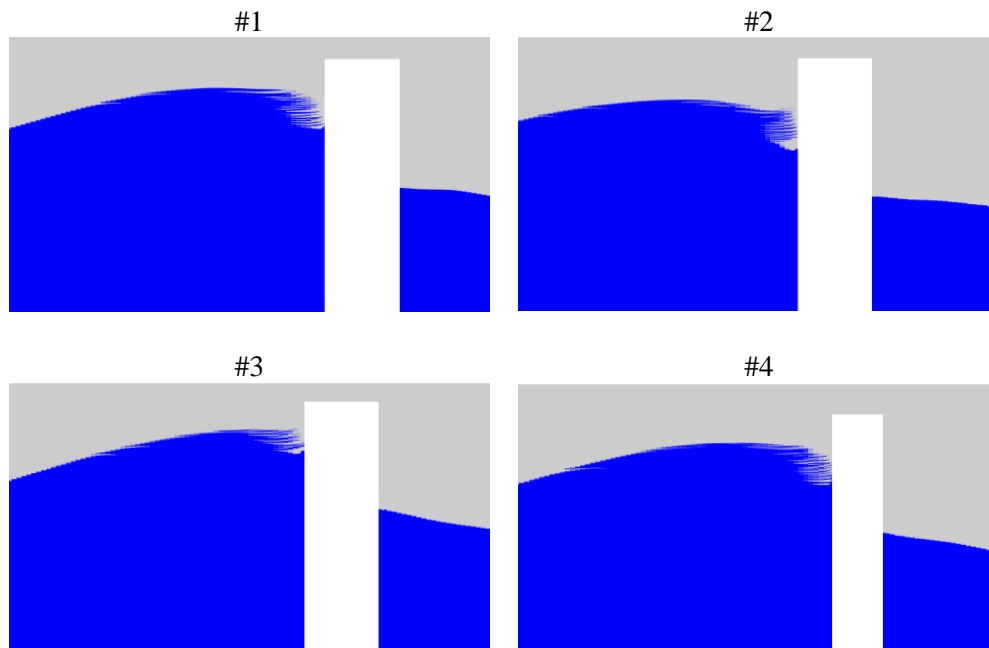
The maximum force caused by each breaking wave is also included in Table 4.1. These peak forces occur when the breaking wave front impacts the front of the structure. Time histories of the inline force on the structure are shown and discussed below in section 5.2.

Table 4.1: Task 4 simulation parameters, including support structure type, unshoaled wave characteristics, and wave characteristics just before breaking and at impact on structure. The last row lists the maximum inline force measured, when the slam impact occurs.

#	1	2	3	4
Structure	10 MW monopile	10 MW monopile	10 MW monopile	5 MW monopile
d_0 (m)	40	40	40	40
H_0 (m)	20	20	25	20
L_0 (m)	250	250	250	250
s (%)	5	5	5	5
2D break loc.	On structure	Before structure	On structure	On structure
d_b (m)	32.01	32.00	31.01	31.68
H_b (m)	18.19	18.19	18.27	17.69
L_b (m)	198.0	197.4	203.5	201.7
d_i (m)	31.06	31.06	29.86	31.06
H_i (m)	16.79	15.65	17.20	16.84
L_i (m)	199.8	178.1	217.8	202.2
$x_i - x_b$ (m)	36.21	54.00	18.25	28.00
Max F (MN)	22.00	24.49	17.88	11.30

Task 5: Comparisons of CFD results to breaking wave limits and load models

The objective of Task 5 is to quantitatively compare breaking wave limits and breaking wave load models to predictions from the CFD simulations carried out in Tasks 3 and 4. First, the McCowan, Miche, Battjes, and Goda breaking limits are evaluated against results from the Task 3 breaking wave simulations. Second, total load predictions based on the Goda, Campbell-Weynberg, Armand-Cointe, and Wienke-Oumerachi breaking wave impact models are evaluated against the results of the Task 4 breaking wave impact simulations.

5.1 Comparison of breaking wave limits

The following four limits are commonly used to predict the maximum wave steepness of a non-breaking wave:

$$\text{McCowan (1894):} \quad \frac{H}{L} = 0.78 \frac{d}{L} \tag{5.1}$$

$$\text{Miche (1944):} \quad \frac{H}{L} = 0.142 \ \tanh\left(2\pi \frac{d}{L}\right) \tag{5.2}$$

$$\text{Battjes (1978):} \quad \frac{H}{L} = 0.142 \ \tanh\left(\frac{0.8}{0.88} \ 2\pi \frac{d}{L}\right) \tag{5.3}$$

$$\text{Goda (1974):} \quad \frac{H}{L_0} = 0.17 \left\{1 - \exp\left[-1.5\pi \frac{d}{L_0}\left(1 + 15 \ s^{\frac{4}{3}}\right)\right]\right\} \tag{5.4}$$

for wave height H (m), wavelength L (m), water depth d (m), seafloor slope s, and deep water wavelength L_0 (m) [15, 16]. The McCowan, Miche, and Battjes limits were developed for water of constant depth d ($s = 0\%$). The McCowan formulation assumed solitary waves, and therefore includes no direct dependence on wavelength L. The Miche formulation assumed periodic waves, as does the Battjes limit which is adapted from the Miche limit. The Goda formulation was developed for waves on a sloped beach and assumes L_0 is the deep water (unshoaled) wavelength, while H and d are measured at breaking [15]. The breaking and non-breaking shoaling regular waves from the Task 3 CFD simulations are used to evaluate the performance of these four breaking limits.

5.1.1 Effect of *H* and *L* characterization

In order to compare the four breaking limits to the CFD simulated waves, the parameters *H, L, d, s,* and L_0 used in the limit formulations must be extracted for each CFD wave. As discussed in section 3.3, there are several different options for measuring the local wavelength and waveheight. These different options for wave height and wavelength characterizations produce markedly different results, as shown in Fig. 5.2. Figure 5.2 compares the accuracy of the criteria for different combinations of *H* and *L* characterizations, by plotting the steepness *H/L* against the

relative depth *d/L* for each simulated wave. Breaking and non-breaking waves are filled and non-filled circles respectively. The limits predicted by the McCowan, Miche, and Goda (for *s*=0% and *s*=12%, using the local breaking *L*) breaking criteria are also shown; the breaking region is above the limit lines. The Battjes limit predicts a slightly lower breaking limit than Miche for all *d/L*, but is nearly identical to Miche and is therefore not included in Fig. 5.2 for visual clarity.
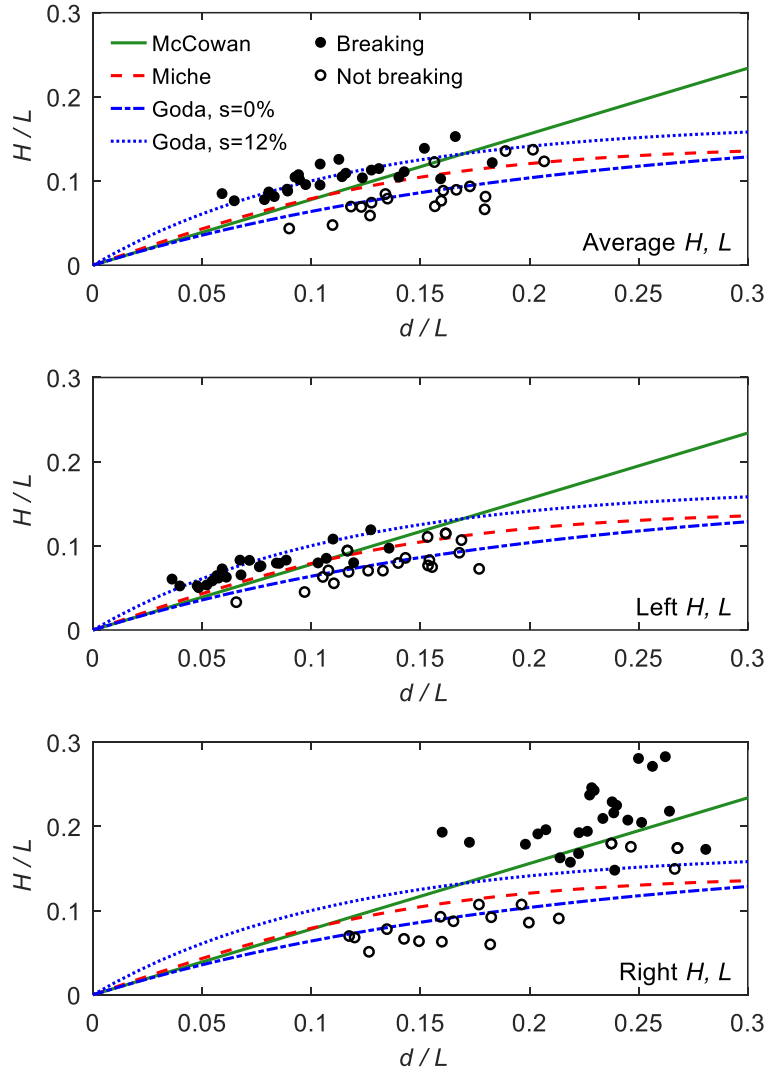
Figure 5.2: Breaking and non-breaking CFD waves (filled and unfilled circles) with McCowan, Miche, and Goda breaking limits (lines). Waves are characterized by the average, left, or right L *and* H *(top, middle, or bottom plot)*

Choosing the average options H_{avg} and L_{avg} (top, Fig. 5.2) works reasonably well for all four breaking limits. The left options H_{left} and L_{left} (middle, Fig. 5.2) and the right options H_{right} and L_{right} (bottom, Fig. 5.2) do not agree as well with the four criteria, although the left options still agree acceptably with the Miche, Battjes, and McCowan limits. Additionally, using H_{right} with L_{avg} also agrees reasonably well with all four limits. For the remainder of the analysis, the average options H_{avg} and L_{avg} are used unless otherwise noted.

Although Fig. 5.2 uses the local, instantaneous wavelength L, the Goda limit was originally derived for the deep water wavelength L_0 rather than the local wavelength L [15, 16]. Figure 5.3 compares the Goda limit to the simulated waves using H_{avg} and the deep water wavelength L_0, for different slope ranges s. The Goda limit matches the CFD results better when the deep water L_0 is used rather than the local L, but only for seafloor slopes $s \leq 8\%$. This slope-dependent accuracy is comparable to the results of Rattanapitikon and Shibayama [16]. In general, the local L is an acceptable alternative in the Goda limit and is preferable for larger seafloor slopes.
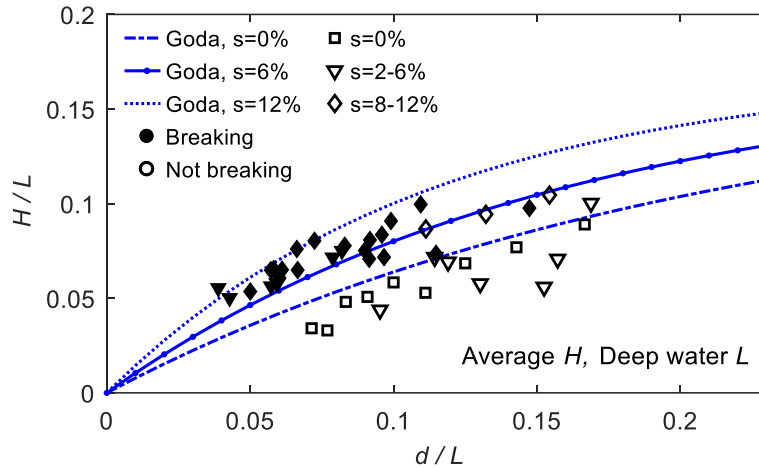
Figure 5.3: Breaking and non-breaking CFD waves (filled and unfilled markers) with Goda breaking limit (lines) for different slopes s. *Waves are characterized by the deep water wavelength* L$_0$ *and average height* H.

5.1.2 Breaking limit performance metrics

The performance of the McCowan, Miche, Battjes, and Goda breaking limits is evaluated by comparing the breaking limit predictions to the CFD simulation results, using the average wavelength and wave height. Figure 5.4 compares the McCowan, Miche, and Goda breaking limits to the breaking and non-breaking CFD waves, grouped by seafloor slope s. Note that the Battjes formulation predicts a slightly lower limit than the Miche limit, but again is not included in Fig. 5.4 for visual clarity. Appendix A also summarizes the data in Figs. 5.3-5.4, and indicates disagreement between the CFD wave and each limit for each wave. When evaluating the four limits' performance in relation to the simulated waves, it is convenient to examine three main ways a limit may be inaccurate when compared with a CFD wave.

First, the limit may predict that a wave should break, although the simulated wave does not. The limit then produces a false positive. Second, the limit may predict that a wave should not break, but the simulated wave does break, producing a false negative. False positives are preferable to false negatives for conservative design purposes, because breaking wave loads are generally higher than non-breaking wave loads [17].

Third, the limit may underpredict the steepness H/L at which a wave breaks, even if it correctly predicts the CFD wave's status at the end of the simulation. This underprediction is quantified by the ratio of the CFD wave's steepness to the limit steepness for a given d/L. Appendix 5.1 also uses this ratio to indicate if the breaking limit prediction agrees with the CFD wave. This steepness underprediction is illustrated when the simulated breaking waves significantly exceed

the breaking criteria's predictions, as shown in Fig. 5.4 and Appendix A, which requires further examination.
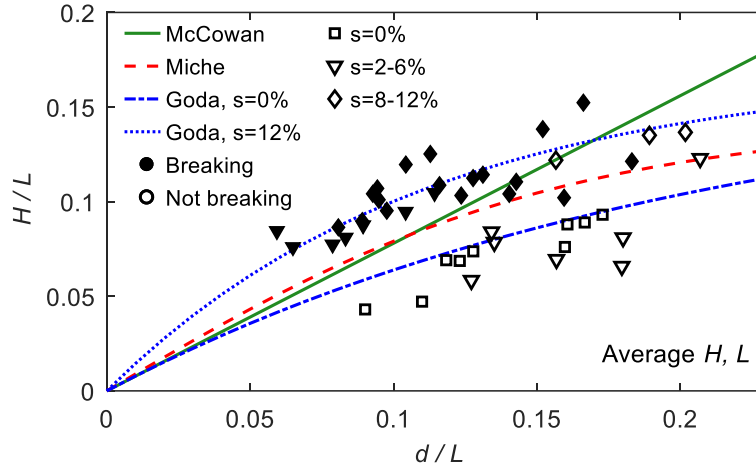

Figure 5.4: Breaking and non-breaking CFD waves (filled and unfilled markers) with McCowan, Miche, and Goda breaking limits (lines) for different slopes s. *Waves are characterized by average wavelength and height.*

5.1.3 Steepness underprediction

In this analysis, waves are identified as breaking when the wave tongue curls over. A few timesteps before a shoaling wave is identified as breaking, the wave had a larger d and L but lower H. Therefore, this slightly earlier version of the simulated wave is not yet breaking, yet still exceeds the breaking limit. There are two possible explanations for this behavior:
   1) breaking is truly initiated significantly before the wave tongue curls over, so that the simulated wave continues to shoal throughout the process of breaking, or
   2) the breaking limits underpredict the steepness H/L at which a wave breaks for a given d/L.
A combination of both explanations is most likely.

Conversely, the simulated non-breaking waves are often significantly below the breaking limits, as shown in Fig. 5.4 and Appendix A. This behavior is physical and expected, since the limits predict an upper bound on non-breaking wave size. For the $s > 0\%$ non-breaking waves, the relatively small waves shown in Fig. 5.4 are simply an artifact of when these waves are measured, at the end of the simulation. With additional domain space and simulation time, presumably these waves would continue to shoal and eventually break.

For $s=0\%$ waves there are no shoaling effects, so that if a wave doesn't immediately break when generated, it will never break during the simulation. Several of the $s=0\%$ wave trains are in fact unstable or breaking when initially generated at the left domain boundary, as predicted by the breaking limits. However, these waves are not included in the breaking wave group because their kinematics are prescribed by stream function theory, which is inaccurate for breaking waves [11], rather than being allowed to develop naturally during the simulation. The stable, smaller waves that form after these initial waves break are recorded as non-breaking, so all simulated $s=0\%$ waves are non-breaking.

5.1.4 Breaking limit performance

Table 5.1 compares the McCowan, Miche, Battjes, and Goda limits based on the occurrence of these three kinds of inaccuracy. The percentage of all recorded waves that are false negatives and false positives are presented for each limit in the first two rows of Table 5.1. The last row shows the average steepness underprediction as a percentage of the CFD breaking steepness.

Table 5.1: Comparison of breaking limit performance based on false negatives, false positives, and steepness underprediction.

Wave breaks?	McCowan	Miche	Battjes	Goda, L	Goda, L_0
Yes, limit says no	9.1%	2.3%	0.0%	9.1%	60.0%
No, limit says yes	0.0%	9.1%	21.0%	6.8%	0.0%
Mean H/L underprediction	23.2%	21.1%	26.6%	13.3%	11.8%

As shown in Table 5.1, none of the limits perform well across all three metrics of accuracy. The Battjes limit has no false negatives and is therefore the most conservative, but tends to significantly underpredict the breaking steepness. The Miche limit also has an acceptably low false negative rate but a lower intermediate false positive rate and steepness underprediction than the Battjes limit. In terms of conservative predictions for design purposes that work for all seafloor slopes, the Battjes and Miche limits have the best overall performance.

The Goda limits with L and the McCowan limit have higher false negative rates than the Miche and Battjes limits, but lower false positive rates (see Table 5.1). The Goda limit with L_0 has the highest false negative rate, although these false negatives only occur for seafloor slopes $s \geq 8\%$, as illustrated in Appendix A. The Battjes and Miche limits are therefore preferable to the McCowan and Goda limits for conservative predictions for design, particularly for large seafloor slopes. However, the Goda limit is preferable for conservative predictions for lower seafloor slopes (see Appendix A), like those found in most of the shallow to intermediate depths off the U.S. East Coast.

Aside from each limit's accuracy, external factors may also influence which limit is best-suited for the design of OWTs. For example, it may be difficult to collect data on the deep water wavelength and sea floor slope required for the full deep water Goda limit with L_0. The Miche and Battjes models' dependence on local wave parameters, without the slope, is advantageous in this respect.

Furthermore, attempts to slightly modify the Battjes and Goda limits did not yield improvements in overall performance. For example, adjusting the coefficients or adding a slope dependence to the Battjes limit may reduce the average steepness overprediction, but increase the number of false negatives. Therefore, the Goda limit with the deep water wavelength should be used for seafloor slopes $s < 8\%$, and the Battjes limit for seafloor slopes $s \geq 8\%$.

5.2 Comparison of breaking wave load models

Wave loads on cylindrical structures, like monopiles, are typically calculated using the Morison equation with drag and inertia terms F_D and F_I respectively. When a breaking wave front slams into the structure, an additional slam term F_S is added to the Morison equation for the force in the direction of wave propagation [18, 19, 20]:

$$F(t) = F_D(t) + F_I(t) + F_S(t) \tag{5.5}$$

This slam term takes the form

$$F_S(t) = \lambda \eta_i \, \rho_w R \, C_p^2 \, C_s(t) \tag{5.6}$$

where λ is the curling factor, η_i is the surface elevation at impact, ρ_w is the density of water, R is the cylinder radius, C_p is the wave celerity, and $C_S(t)$ is the time-varying slam coefficient [18, 19]. The term $\lambda \eta_i$ is a measure of the height affected by the slamming force; values of 0.4 to 0.5 for λ for plunging breakers are typically cited from Goda et al.'s 1966 work [20].

However, there are several disagreeing models for the slam coefficient $C_S(t)$. Four of the most popular are described in Table 5.2: Goda 1966, Campbell-Weynberg 1980 (C-W), Cointe-Armand 1987 (C-A), and Wienke-Oumerachi 2005 (W-O) [18, 19]. These four models predict different slam durations Δt_S, different shapes for the $C_S(t)$ curve, and different values for the maximum slam force. Note that all four models predict a peak C_S (and therefore a peak slam force) at the beginning of the slam force time history, when $t_s = 0$.

In this section, the breaking wave forces calculated in the Task 4 CFD simulations are compared to the predictions made by these four models in conjunction with the Morison equation (Eqns. 5.5-5.6).

Table 5.2: Common slam force models, their predicted slam durations Δt_S, and their predicted slam coefficient time histories $C_S(t)$. Bolded values indicate the maximum predicted slam coefficient. Adapted from [19].

Slam model	Duration Δt_S	Coefficient $C_S(t_s)$: **bold** = max. value
Goda	$\dfrac{R}{C_p}$	$\boldsymbol{\pi\left(1-\dfrac{C_p t_s}{R}\right)}$
Campbell-Weynberg	$\dfrac{2R}{C_p}$	$\boldsymbol{5.15}\left(\dfrac{R}{R+9.5 C_p t_s}+\dfrac{0.0535 C_p t_s}{R}\right)$
Cointe-Armand	$\dfrac{3R}{C_p}$	$\boldsymbol{2\pi}-\left(4.72-\ln\left(\dfrac{C_p}{R}t_s\right)\right)\sqrt{\dfrac{C_p}{R}t_s}$
Wienke-Oumerachi	$\dfrac{13R}{32 C_p}$	$\boldsymbol{2\pi}-2\sqrt{\dfrac{C_p}{R}t_s}\tanh^{-1}\sqrt{1-\dfrac{C_p t_s}{4R}},\qquad\qquad\text{for } 0\le t_s\le\dfrac{R}{8 C_p}$ $\pi\sqrt{\dfrac{R}{6 C_p t_s{}'}}-\sqrt[4]{\dfrac{8}{3}\dfrac{C_p}{R}t_s{}'}\tanh^{-1}\sqrt{1-\dfrac{C_p}{R}t_s{}'\sqrt{\dfrac{6 C_p}{R}t_s{}'}},\quad\text{for }\dfrac{R}{8 C_p}\le t_s\le\dfrac{13R}{32 C_p}$ $\text{where } t_s{}'=t-\dfrac{R}{32 C_p}$

5.2.1 Calculating drag and inertia terms

Although the slam force is separated from the drag and inertia forces in the Morison equation (see Eqn. 5.5), the simulated CFD force is the combined total inline force (in the direction of wave propagation). The inline drag and inertia forces must therefore also be predicted using the Morison equation in order to compare the slam coefficient models to the CFD force. This approach would also be used to predict the total load a support structure would experience due to a breaking wave of known characteristics.

The inline drag force on the cylinder is predicted from the CFD horizontal fluid velocities $u(z,t)$, by summing up the inline force per unit length over dz-tall segments of the cylinder. The total inline drag force on the cylinder is then given by

$$F_D(t) = \sum_{z=floor}^{z=interface}[1-\alpha(z,t)]\rho_w R\, u(z,t)|u(z,t)|\, C_D\, \mathrm{d}z \qquad (5.7)$$

where the water density ρ_w is weighted by the void fraction α to account for cells that are not fully water ($\alpha = 0.0$). The drag coefficient C_D is estimated for each of the Task 4 CFD simulations by extrapolating from the commonly cited Sarpkaya experimental curves for C_D as a function of Reynolds number Re and Keulegan-Carpenter number KC [22].

The CFD $u(z,t)$ is measured at the x-location of the structure leading edge, at a y-location of $4R$ from the structure center. Since the wave form is uniform in y until it interacts with the structure, this approximates the wave kinematics at the structure location as if no structure existed. This approach is akin to obtaining breaking wave kinematics for a known wave (from measurements, wave theory approximations, or CFD) and predicting the force on a theoretical structure using the Morison equation. Using the structure leading edge as the x-location for the $u(z,t)$ measurement, rather than the structure center, was found to better capture the gradual rise in force prior to the slamming impact.

The inline inertia force on the cylinder is predicted from the CFD horizontal fluid acceleration $a_x(z,t)$ using a similar summing approach as the drag force:

$$F_I(t) = \sum_{z=floor}^{z=interface} [1 - \alpha(z,t)]\rho_w \ \pi R^2 \ a_x(z,t) \ C_M \ dz \qquad (5.8)$$

where the inertia coefficient C_M is again estimated for each CFD wave using Sarpkaya's experimental C_M (*Re, KC*) curves [22]. The CFD $a_x(z,t)$ is estimated from the same $u(z,t)$ used in the drag calculation using a central difference approximation for the derivative. This represents the undisturbed horizontal acceleration at the location of the structure's leading edge.

Table 5.3 summarizes the parameter values used to calculate the predicted drag and inertia force for each CFD wave, including the cylinder segment height dz Reynolds number Re, Keulegan-Carpenter number KC, and the estimated drag and inertia coefficients C_D and C_M. For each simulated wave, the cylinder segment height dz = 0.075 m is equal to the cell size at the air-water interface.

The wave celerity C_p and surface elevation at impact η_i used to calculate the predicted slam force in Eqn. 5.6 are also included in Table 5.3. Values for C_p and η_i are calculated from CFD surface elevation snapshots, again located at $y = 4R$ to approximate a wave without a structure. A value of $\lambda = 0.4$ is used for the curling factor for all four simulated waves.

Table 5.3: Parameter values used to predict drag, inertia, and slam forces in Eqns. 5.6-5.8 for each simulated wave. See Table 4.1 for additional information on each wave.

#	Max. CFD F (MN)	Re	KC	C_D	C_M	C_p (m/s)	η_i (m)
1	22.00	1.8 x 10^8	33	0.71	1.74	17.44	13.03
2	24.49	1.8 x 10^8	32	0.71	1.74	17.98	12.22
3	17.88	1.9 x 10^8	31	0.71	1.74	18.88	13.82
4	11.30	1.2 x 10^8	48	0.68	1.76	17.48	13.01

5.2.2 Comparison of force time histories

Using Eqns. 5.7-5.8 and the values listed in Table 5.3, the drag and inertia forces predicted by the Morison equation are calculated for each simulated CFD wave. The slam force is also calculated for each CFD wave, using each of the four slam coefficient models listed in Table 5.2. The predicted total inline force time history (drag plus inertia plus slam) is then compared to the CFD total inline force time history for each wave. Figures 5.5-5.8 compare the CFD (black curve) and predicted total force time histories for each of the four slamming coefficient models (colored curves). The predicted drag and inertia force time histories are also included in Figs. 5.5-5.8.

As shown in Figs. 5.5-5.8, the predicted total inline force matches the CFD total force reasonably well for the times leading up to the impact in each case. The inertia force dominates the predicted

total force until the times immediately before the impact, when the fast-moving wave crest contributes to a larger predicted drag force.

At impact, all four slam coefficient models predict a higher peak total force than the CFD model, although Goda is the closest with the lowest peak slam coefficient (see Figs. 5.5-5.8). This could partially be caused by numerical dispersion in the wave crest in the CFD simulations, where the fast-moving crest is artificially spread out (see Fig. 4.3) which causes the slam force to be lower in magnitude but larger in duration.

After the initial impact, the four slam models vary significantly due to their different slam durations (see Figs. 5.5-5.8). For example, the W-O slam model tends to predict a total force lower than the CFD force after the initial impact due to its short slam duration, while C-A slam model tends to predict a higher post-impact force than the CFD, due to C-A's longer slam duration.

Of the four CFD simulations, some feature a distinct slam force more clearly than others. In particular, simulation #2 most clearly displays a sharp slam force (Fig. 5.6), and a smaller slam force is also evident in simulation #3 (Fig. 5.7). Simulations #1 and #4 (Figs. 5.5 and 5.8) also show a sharp increase in force when the wave front impacts the structure, although it does not decay quickly after impact as would be expected with a slam force. However, this increase in force is only partially captured using drag and inertia models alone, indicating that some slam force is present.

Figure 5.5: Inline force time history for Task 4 simulation #1 (10 MW monopile), including CFD total force (black curve), predicted inertia and drag (dashed stars and crosses), and predicted total force using Goda (cyan squares), Campbell-Weynberg (green downward triangles), Cointe-Armand (blue upward triangles), and Wienke-Oumerachi (red diamonds) slam coefficient models.
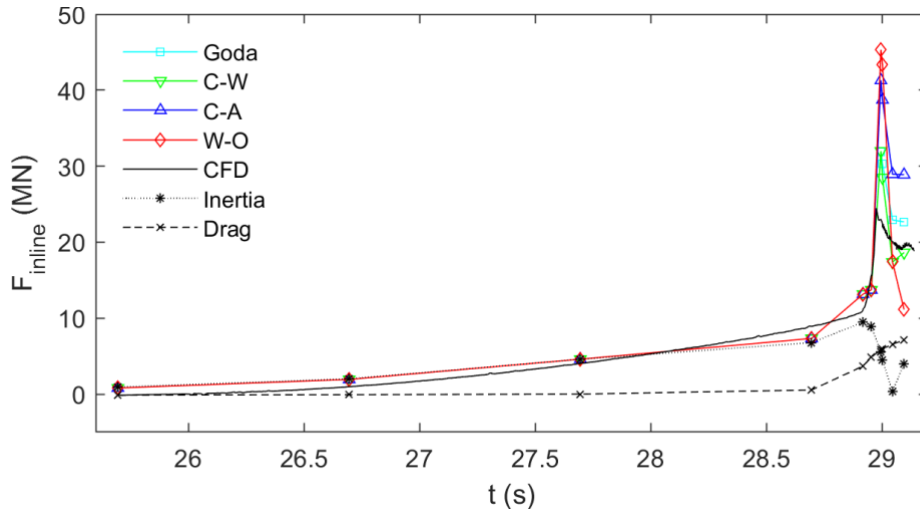
Figure 5.6: Inline force time history for Task 4 simulation #2 (10 MW monopile), including CFD total force (black curve), predicted inertia and drag (dashed stars and crosses), and predicted total force using Goda (cyan squares), Campbell-Weynberg (green downward triangles), Cointe-Armand (blue upward triangles), and Wienke-Oumerachi (red diamonds) slam coefficient models.
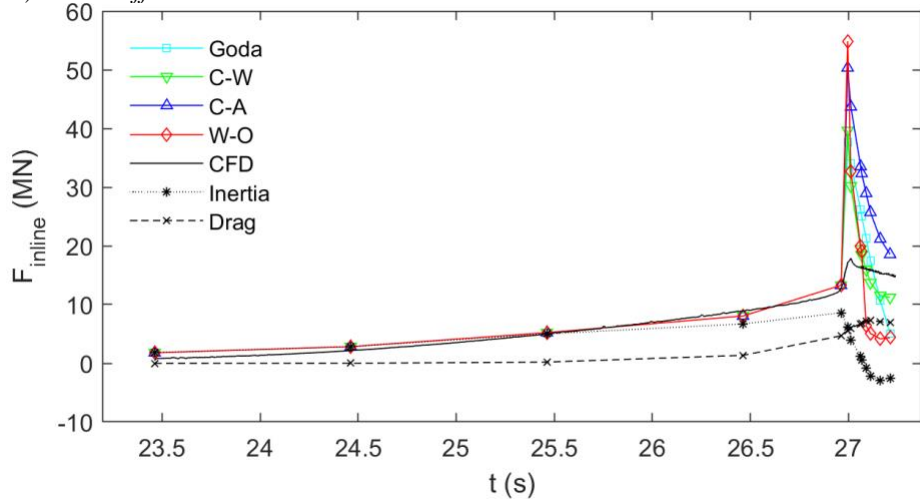
Figure 5.7: Inline force time history for Task 4 simulation #3 (10 MW monopile), including CFD total force (black curve), predicted inertia and drag (dashed stars and crosses), and predicted total force using Goda (cyan squares), Campbell-Weynberg (green downward triangles), Cointe-Armand (blue upward triangles), and Wienke-Oumerachi (red diamonds) slam coefficient models.
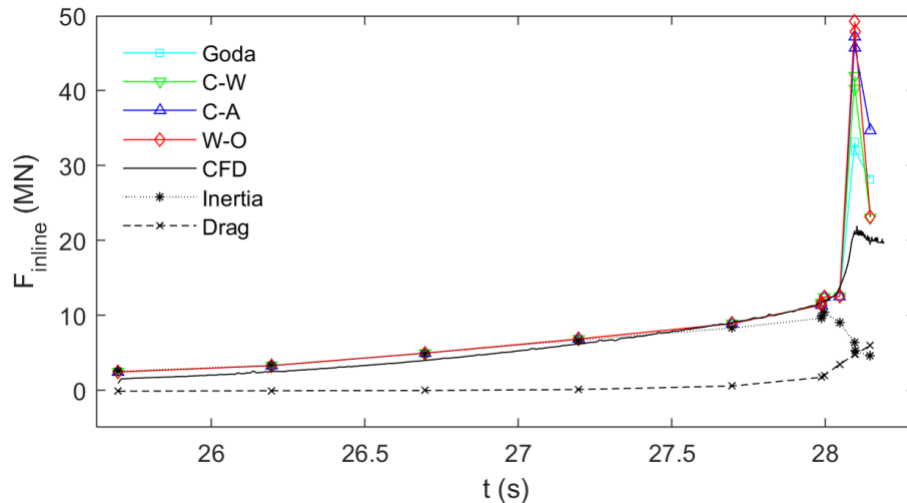
Figure 5.8: Inline force time history for Task 4 simulation #4 (5 MW monopile), including CFD total force (black curve), predicted inertia and drag (dashed stars and crosses), and predicted total force using Goda (cyan squares), Campbell-Weynberg (green downward triangles), Cointe-Armand (blue upward triangles), and Wienke-Oumerachi (red diamonds) slam coefficient models.
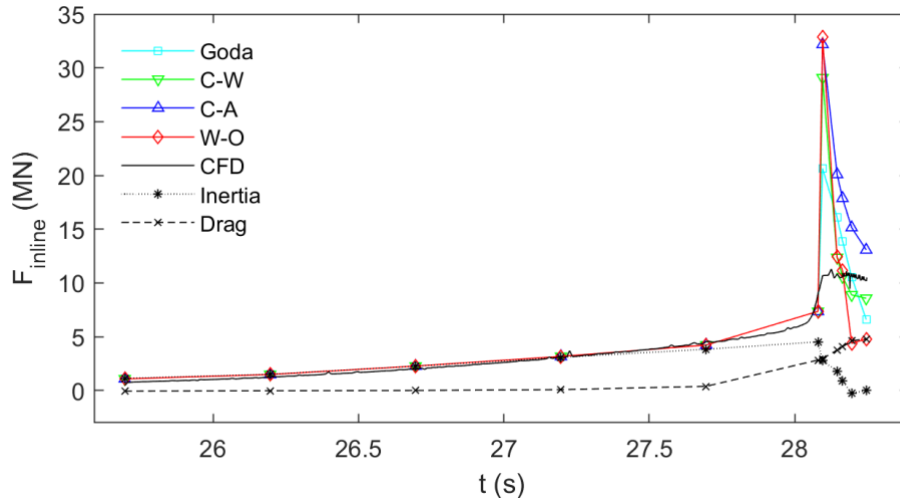
The differences in CFD force time history between the four simulated waves are strongly dependent on wave structure at the time of impact. As shown in Table 4.1, the four waves are extremely similar just before breaking. However, the waves are still in the process of breaking when they impact the structures; the stage of breaking has a significant effect on the force.

As discussed in section 4.4, simulations #2 and #3 are farther along in the breaking process than simulations #1 and #4, so that more of the crest is moving as a vertical wall of water (see Fig. 4.3). This creates the more distinct slamming force peak, and is consistent with the idea that the highest force occurs when the crest has turned into a vertical wall of water impacting the cylinder [20].

5.2.3 Comparison of slam coefficients

To gain additional insight into how the slam coefficient models compare to each other and to the CFD results, a CFD-based slam coefficient $C_s(t)$ is calculated for each case using the total CFD force and the predicted drag and inertia forces. Figure 5.9 plots the slam coefficient time histories for the four slam coefficient models (colored curves) alongside the CFD-based $C_S(t)$ (black circles). Markers indicate the times where drag and inertia forces are calculated, limited to the times of recorded snapshots of the CFD fluid velocity $u(z,t)$.

As illustrated in Fig. 5.9, none of the four models for $C_S(t)$ capture the CFD force beyond the predicted drag and inertia terms well. Simulations #3 and #4 in particular feature a sustained, slightly increasing CFD force beyond the initial time of impact. None of the four $C_S(t)$ models fit this shape, likely because the sustained CFD force is caused less by the slamming impact and more due to a continued imbalance in surface elevation across the cylinder. This sustained elevated force can also be seen for all the simulated waves (see Figs. 5.5-5.8), even those with identifiable slam force (see Figs. 5.6-5.7). Improved models for drag and inertia, or perhaps

32

adding an additional term to the Morison force equation, may address this portion of the force better than any slam-focused model.
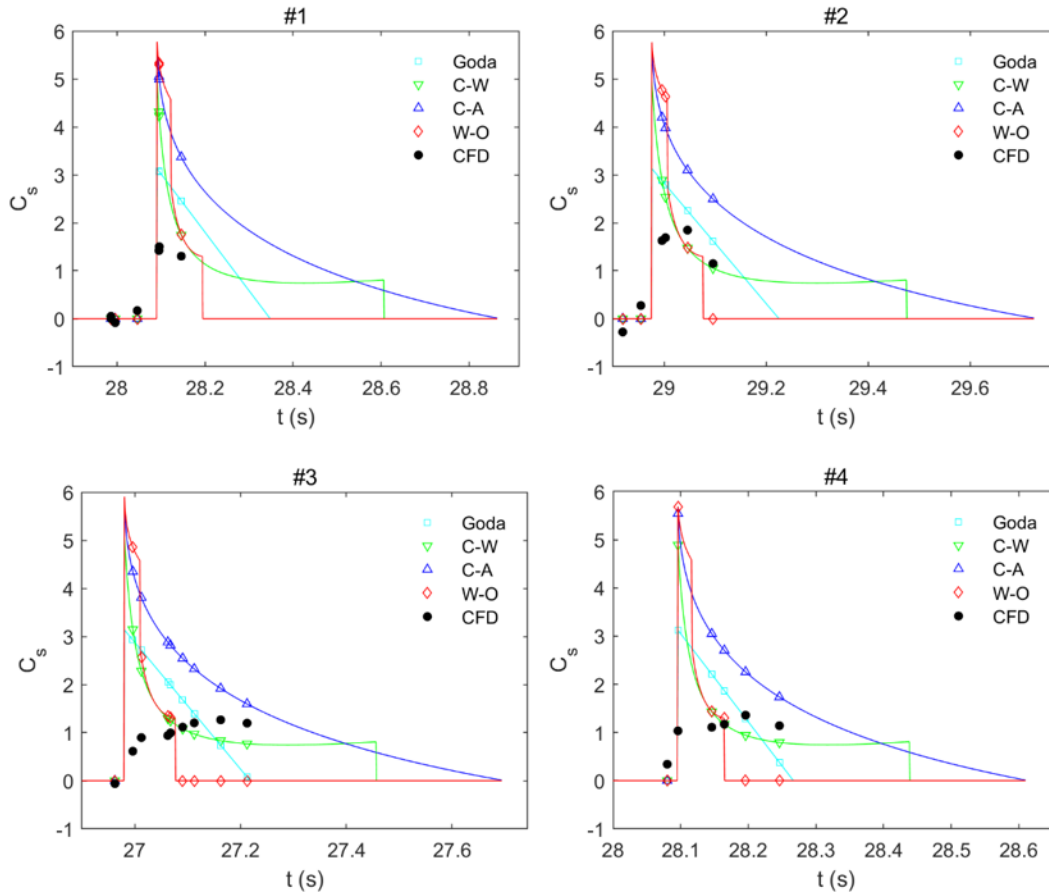
Figure 5.9: Slam coefficient time histories for Task 4 simulations #1 (top left), #2 (top right), #3 (bottom left), and #4 (bottom right). Slam coefficients are calculated using the Goda (cyan squares), Campbell-Weynberg (green down triangles), Cointe-Armand (blue up triangles), and Weinke-Oumerachi (red diamonds) models, as well as based on the CFD total force (filled black circles).

Aside from the shape of the slamming coefficient time history, the maximum total force should also be accurately predicted by the slamming coefficient models when used in conjunction with the Morison equation. However, as noted in Figs. 5.5-5.8, the maximum CFD total force is significantly below the predicted peak force using the four slam models, even for the simulations with clear slam forces. Table 5.4 compares the peak inline force for the total CFD force, the CFD slam force based on interpolated values for the predicted drag and inertia, and the predicted slam force using all four slamming coefficient models. The ratio between the predicted slam force and the CFD slam force is reported in parentheses for each model and each simulated wave.

A CFD-based maximum C_S is also included in Table 5.4, based on the peak CFD C_S using the same $\lambda=0.4$ used throughout this report. The last column in Table 5.4 factors out the curling factor λ to give a single dimensionless parameter λC_S that is theoretically constant across all waves.

Table 5.4: Comparing maximum values for CFD total force, CFD slam force, and predicted slam force. Slamming coefficient and single fit parameter λC_S are reported based on CFD slam force. Values in parentheses are relative to CFD slam force.

#	CFD F (MN)	CFD F_S (MN)	Goda F_S (MN)	C-W F_S (MN)	C-A, W-O F_S (MN)	CFD C_S, λ=0.4	CFD λC_S
1	22.00	11.81	22.41 (1.9x)	36.74 (3.1x)	44.82 (3.8x)	1.66	0.662
2	24.49	11.95	22.34 (1.9x)	36.62 (3.1x)	44.67 (3.1x)	1.68	0.673
3	17.88	7.96	27.87 (3.5x)	45.68 (5.7x)	55.73 (5.7x)	0.897	0.359
4	11.30	5.67	14.98 (2.6x)	24.56 (2.6x)	29.97 (4.3x)	1.19	0.476

As Table 5.4 illustrates, all four models predict a peak slam force several times larger than the CFD peak slam force. Goda is the closest to the peak CFD slam force, followed by Campbell-Weynberg, followed by Cointe-Armand and Wienke-Oumerachi.

5.2.4 Limitations of existing slam models

As indicated in Table 5.4 as well as Figs. 5.5-5.9, the existing slam models significantly disagree with the simulated forces for these four breaking waves. According to the CFD peak slam forces, a lower value for the peak $C_S(t)$ should be used (see Table 5.4), or perhaps a lower value for the factor λC_S since very little guidance is given on the curling factor. The variation in the peak λC_S across the four simulated waves indicates that one or more important factors are neglected in the existing slam model formulations.

For instance, cylinder runup is not explicitly accounted for in the existing slam models, although it is present in all four simulations (see Fig. 4.3). Using the horizontal velocity $u(z,t)$ and acceleration $a_x(z,t)$ as measured at the cylinder leading edge (rather than the cylinder center) for Morison drag and inertia does capture the effect of runup acceptably, at least before wave impact, as shown in Figs. 5.5-5.8. However, the effects of runup post-impact could explain the sustained elevated force post-impact observed in all four simulated waves. None of the four existing models for slam capture this effect, as shown in Figs. 5.5-5.9.

Additionally, the existing slam models assume the breaking wave is a plunging breaker, with the moment of impact occurring when the wave front is vertical. While this scenario produces the highest peak force, it does not address breaking waves at other stages of breaking, as reflected in Table 5.4 and Figs. 5.5-5.9.

Overall, these CFD simulations indicate that the existing slam force models provide a strongly conservative prediction for the peak inline force due to breaking waves. However, the predicted time history of the total breaking force could be further improved by including runup effects. These four slam force models in conjunction with traditional Morison drag and inertia do not account for the variety of breaking wave shapes and impact timings, but provide a conservative estimate for most breaking waves.

Project conclusions

In summary, four breaking wave limits and four slam force models are evaluated using CFD simulations of breaking waves with characteristics representative of potential East Coast offshore wind energy sites. First, representative extreme ocean conditions for three East Coast sites are described. Second, the CFD model used in the simulations is developed in a series of validation and verification studies, including wave generation and absorption, wave shoaling and breaking, and wave forces on a cylinder. Third, four breaking wave limits (McCowan, Miche, Battjes, and Goda) that predict if a wave will break are evaluated using 39 CFD simulations of shoaling and breaking waves. Fourth, four slam force models (Goda, Campbell-Weynberg, Cointe-Armand, and Wienke-Oumerachi) that predict the force on a cylinder due to breaking waves are evaluated using four CFD simulations of waves shoaling and breaking on monopiles designed for 5 and 10 MW offshore wind turbines.

When examining the breaking wave limits, this project concludes that:

- The Goda limit is the most accurate breaking limit for low seafloor slopes ($s < 8\%$), which are common at East Coast sites suitable for fixed-bottom offshore wind farms.
- The Miche and Battjes limits are acceptable conservative alternatives that perform reasonably for a wider range of seafloor slopes.
- Simple modifications to the Goda and Battjes limits do not yield improved overall performance.
- The performance of each limit depends on how the wave height and wavelength are measured in an asymmetric shoaling wave.

Regarding the force predictions from slam force models, this project indicates that:

- All four slam force models are conservative and assume the "worst case" shape for the breaking wave during impact. Less conservative models should account for different wave shapes during impact by adjusting the value of λC_S.
- When predicting peak impact force, the Goda slam model is generally the least conservative, while the Cointe-Armand and Wienke-Oumerachi slam models are generally the most conservative.
- All four slam force models do not capture the total force time history well after the initial impact, potentially due to neglecting the effects of runup on the monopile.

In conclusion, this work indicates that the Goda breaking wave limit should be used to predict if a wave will break for seafloor slopes less than 8%, and the Battjes limit should be used to conservatively predict if a wave will break for seafloor slopes greater than 8%. Furthermore, the Wienke-Oumerachi or Cointe-Armand slam force models are good choices for highly conservative predictions of the peak impact force due to a breaking wave.

References

1. Hervey, R.V. (2013). *Documentation for the National Data Buoy Center Coastal-Marine Automated Network and moored (weather) buoy data* [dataset]. National Oceanographic Data Center #0070493, NOAA.
2. Hesser, T. (2010). *U.S. Army Corps of Engineers Wave Information Studies project documentation* [dataset]. Coastal and Hydraulics Laboratory, U.S. Army Corps of Engineers.
3. International Electrotechnical Commission (2005). *Wind turbines – part 1: Design requirements.* IEC 61400-3.
4. *U.S. coastal relief model, northeast Atlantic* [dataset]. (1999). National Geophysical Data Center, NOAA. DOI:10.7289/V5MS3QNZ
5. *U.S. coastal relief model, southeast Atlantic* [dataset]. (1999). National Geophysical Data Center, NOAA. DOI:10.7289/V53R0QR5.
6. QGIS development team. (2017). *QGIS geographic information system.* Open Source Geospatial Foundation Project.
7. Whitman, G. B. (1974). *Linear and nonlinear waves*. John Wiley & Sons, New York.
8. Richards, K. J., Senecal, P. K., and Pomraning, E. (2018). *Converge v2.4 manual.* Convergent Science Inc., Madison, WI.
9. Fenton, J.D. (1985). A fifth-order Stokes theory for steady waves. *J. Waterway, Port, Coastal, Ocean Eng.,* 111(2), 216–234.
10. Fenton, J.D. (1990). Nonlinear wave theories. *The Sea: Ocean Engineering Science*, 9, 3–25. Retrieved from http://johndfenton.com/Papers/Fenton90b-Nonlinear-wave-theories.pdf.
11. Fenton, J.D. (1988). The numerical solution of steady water wave problems. *Computers and Geosciences* 14(3), 357-368. DOI 10.1016/0098-3004(88)90066-0.
12. Niedzwecki, J. M., and Duggal, A. S. (1992). Wave runup and force on cylinders in regular and random waves. *J. Waterway, Port, Coastal, Ocean Eng.,* 118(6), 615–634.
13. Velarde, J. (2016). *Design of monopile foundations to support the DTU 10 MW wind turbine.* Master's thesis, Delft University of Science and Technology and Norwegian University of Science and Technology.
14. de Vries, W. (2011). *Support structure concepts for deep water sites*. Deliverable D4.2.8 (WP 4.2 Final Report), Project UpWind.
15. Jensen, M.S. (2004). *Breaking of waves over a steep bottom slope.* Hydraulics & Coastal Engineering Laboratory, Dept. of Civil Engineering, Aalborg University. Series paper, no. 22.
16. Rattanapitikon, W. and Shibayama, T. (2000). Verification and modification of breaker height formulas. *Coastal Engineering* 42(4), 389-406. DOI 10.1016/S0578-5634(00)00019-5.
17. Chella, Mayilvahanan. (2016). *Breaking Wave Characteristics and Breaking Wave Forces on Slender Cylinders.* PhD thesis, Norwegian University of Science and Technology, Trondheim, Norway.
18. Hallowell, S., Myers, A., and Arwade, S. (2015). Variability of breaking wave characteristics and impact loads on offshore wind turbines supported by monopiles. *Wind Energy* 19(2), 301-312. DOI 10.1002/we.1833.
19. Tu, Y., Cheng, Z., and Muskulus M. (2017). A review of slamming load application to offshore wind turbines from an integrated perspective. *Energy Procedia* 137, 346-357. DOI 10.1016/j.egypro.2017.10.359.

20. Wienke, J. and Oumeraci, H. (2005). Breaking wave impact force on a vertical and inclined slender pile – theoretical and large-scale model investigations. *Coastal Eng* 52(5), 435-462. DOI doi:10.1016/j.coastaleng.2004.12.008.
21. Sarpkaya, T. (2010). *Wave force on offshore structures.* Cambridge University Press, Cambridge.

Appendix A: Breaking wave limit data

Wave parameters using the average wave height H_{avg} and average wavelength L_{avg} are listed for individual simulated waves. The ratios of the simulated H/L to the predicted breaking H/L for the McCowan, Miche, Battjes, and Goda (both local L and deep water L_0) limits are presented in the last four columns. Boldface ratios indicate disagreement between the simulated wave and the breaking limit.

Breaking waves

s (%)	d (m)	H (m)	L (m)	d/L	H/L	McCowan	Miche	Battjes	Goda, L	Goda, L_0
5	21.4	25.1	329.8	0.065	0.076	1.50	1.38	1.51	1.38	1.30
5	32.1	31.5	407.5	0.079	0.077	1.26	1.19	1.29	1.21	1.14
6	12.2	17.4	206.4	0.059	0.084	1.83	1.67	1.82	1.58	1.48
6	11.6	11.3	139.4	0.083	0.081	1.25	1.19	1.29	1.16	1.08
6	18.7	18.3	208.7	0.089	0.088	1.26	1.21	1.31	1.19	1.09
6	21.7	19.7	207.9	0.104	0.095	1.16	1.16	1.25	1.15	1.07
6	2.9	2.6	25.1	0.114	0.105	1.17	1.20	1.28	1.19	1.08
8	21.7	21.8	243.4	0.089	0.090	1.29	1.24	1.35	1.12	1.02
8	42.8	45.6	451.1	0.095	0.101	1.36	1.33	1.44	1.21	1.08
8	21.6	18.0	174.8	0.124	0.103	1.07	1.12	1.20	1.04	**0.93**
9	32.9	32.1	337.4	0.098	0.095	1.25	1.23	1.32	1.07	**0.97**
9	21.6	18.8	164.6	0.131	0.114	1.12	1.19	1.27	1.07	**0.95**
9	2.4	1.8	17.2	0.140	0.104	**0.95**	1.04	1.10	**0.94**	0.81
9	2.3	1.8	16.0	0.143	0.110	**0.99**	1.09	1.16	**0.98**	0.83
9	2.9	1.8	18.0	0.159	0.102	**0.82**	**0.94**	1.00	**0.86**	0.74
9	15.5	10.3	84.5	0.183	0.121	**0.85**	1.04	1.09	**0.95**	0.85
11	12.0	12.9	148.7	0.081	0.086	1.37	1.30	1.41	1.03	**0.91**
11	33.2	31.1	286.1	0.116	0.109	1.20	1.23	1.32	1.02	**0.91**
11	36.7	32.3	287.4	0.128	0.112	1.13	1.19	1.27	1.00	**0.88**
11	39.6	36.3	238.5	0.166	0.152	1.17	1.38	1.45	1.19	**0.94**
12	3.8	4.2	40.8	0.093	0.104	1.44	1.40	1.51	1.09	**0.95**
12	18.0	20.4	191.0	0.094	0.107	1.45	1.42	1.53	1.11	**0.96**
12	20.9	23.9	200.2	0.104	0.120	1.47	1.46	1.58	1.16	1.00
12	27.9	30.9	247.2	0.113	0.125	1.42	1.45	1.55	1.16	**1.00**
12	13.7	12.5	90.0	0.152	0.138	1.17	1.31	1.39	1.10	**0.94**

Non-breaking waves

s (%)	d (m)	H (m)	L (m)	d/L	H/L	McCowan	Miche	Battjes	Goda, L	Goda, L_0
0	10.0	4.8	111.0	0.090	0.043	0.61	0.59	0.64	0.73	--
0	25.0	10.7	227.4	0.110	0.047	0.55	0.55	0.60	0.69	--
0	30.0	17.5	253.4	0.118	0.069	0.75	0.77	0.83	0.95	--
0	5.0	2.8	40.6	0.123	0.069	0.72	0.75	0.80	0.92	--
0	50.0	28.8	391.2	0.128	0.074	0.74	0.78	0.83	0.96	--
0	45.0	21.4	281.7	0.160	0.076	0.61	0.70	0.74	0.85	--
0	40.0	21.9	249.0	0.161	0.088	0.70	0.81	0.85	0.97	--
0	20.0	10.7	120.0	0.167	0.089	0.68	0.80	0.85	0.96	--
0	35.0	18.8	202.4	0.173	0.093	0.69	0.82	0.87	0.98	--
2	54.9	34.4	409.0	0.134	0.084	0.80	0.86	0.92	1.00	0.95
2	13.0	5.8	83.0	0.157	0.069	0.57	0.65	0.68	0.74	0.70
2	36.6	13.4	203.8	0.180	0.066	0.47	0.57	0.60	0.65	0.61
3	15.7	7.2	123.7	0.127	0.058	0.59	0.62	0.66	0.69	0.64
3	69.6	40.5	515.2	0.135	0.079	0.75	0.80	0.85	0.90	0.86
3	7.1	3.2	39.3	0.180	0.081	0.58	0.70	0.74	0.77	0.73
5	27.0	16.0	130.6	0.207	0.123	0.76	**1.00**	**1.04**	**1.01**	0.92
8	22.3	17.3	142.1	0.157	0.122	1.00	**1.14**	**1.20**	**1.06**	0.93
8	12.3	8.4	61.2	0.202	0.137	0.87	**1.13**	**1.18**	**1.05**	0.92
12	17.8	12.7	94.3	0.189	0.135	0.92	**1.15**	**1.20**	0.98	0.80

Appendix B: Variable definitions

α	Void fraction: 0.0 = water, 1.0 = air	[]
γ	JONSWAP peak shape parameter	[]
Δt_s	Slamming force duration	[s]
η	Water surface elevation above still water level	[m]
ρ	Fluid density	[kg/m^3]
σ	JONSWAP scaling factor	[]
a	Cylinder radius, Niedzwecki & Duggal experiments	[m]
d	Water depth	[m]
d_0	Height of initial dammed water, nominal water depth	[m]
d_b	Water depth just before breaking	[m]
d_i	Water depth at time of impact on structure	[m]
f	Wave frequency	[Hz]
g	Gravitational acceleration	[m/s^2]
k	Wavenumber	[m^{-1}]
m_i	i^{th} spectral moment of wave spectrum	[*varies*]
s	Seafloor slope	[%]
t	Time	[s]
t_s	Time since slamming impact	[s]
$\boldsymbol{u}$	Fluid velocity vector	[m/s]
u	Horizontal fluid velocity, in direction of wave propagation	[m/s]
w	Initial width of dammed water	[m]
x	Location coordinate, in direction of wave propagation	[m]
x_b	Wave crest location just before breaking	[m]
x_i	Wave crest location at time of impact on structure	[m]
z	Location coordinate in the vertical direction	[m]
C_D	Drag coefficient used to model F_D	[]
C_M	Inertia coefficient used to model F_I	[]
C_p	Wave celerity	[m/s]
C_S	Slam coefficient used to model F_S	[]
F	Total inline force on structure	[N]
F_D	Inline drag force on structure	[N]
F_I	Inline inertia force on structure	[N]
F_{inline}	Force on structure in direction of wave propagation	[N]
F_S	Inline slam force on structure due to breaking wave	[N]
H	Wave height, general	[m]
H_0	Nominal or deep water wave height	[m]
H_{avg}	Average of H_{left} and H_{right}	[m]
H_b	Wave height just before breaking	[m]
H_i	Wave height at time of impact on structure	[m]
H_{left}	Wave height using left trough	[m]
H_{right}	Wave height using right trough	[m]
H_s	Significant wave height	[m]
KC	Keulegan-Carpenter number	[]
L	Wavelength, general	[m]
L_0	Nominal or deep water wavelength	[m]
L_{avg}	Trough to trough wavelength	[m]
L_b	Wavelength just before breaking	[m]
L_i	Wavelength at time of impact on structure	[m]
L_{left}	Wavelength using left trough	[m]
L_{right}	Wavelength using right trough	[m]
R	Monopile radius	[m]
Re	Reynolds number	[]
S	Momentum sink coefficient	[Hz]
$S(f)$	Wave spectral density, as function of frequency	[m^{2}s]
T	Wave period, general	[s]
T_{avg}	Average wave period	[s]
T_p	Wave peak spectral period	[s]